

AD-A245 995



# NAVAL POSTGRADUATE SCHOOL

## Monterey, California

2



## THESIS

A COMPARISON OF HIGH-LATITUDE IONOSPHERIC  
PROPAGATION PREDICTIONS FROM  
ADVANCED PROPHET 4.0 WITH MEASURED DATA

by

Stefanos S. Gikas

Thesis Advisor:

Richard W. Adler

Approved for public release; distribution is unlimited

92 2 12 043

92-03564



CLASSIFIED

SECURITY CLASSIFICATION OF THIS PAGE

## REPORT DOCUMENTATION PAGE

Form Approved  
OMB No. 0704-0188

REPORT SECURITY CLASSIFICATION <b>CLASSIFIED</b>		1b RESTRICTIVE MARKINGS	
SECURITY CLASSIFICATION AUTHORITY		3. DISTRIBUTION/AVAILABILITY OF REPORT Approved for public release; distribution is unlimited	
DECLASSIFICATION/DOWNGRADING SCHEDULE		5 MONITORING ORGANIZATION REPORT NUMBER(S)	
PERFORMING ORGANIZATION REPORT NUMBER(S)		7a. NAME OF MONITORING ORGANIZATION Naval Postgraduate School	
NAME OF PERFORMING ORGANIZATION Naval Postgraduate School		6b OFFICE SYMBOL (if applicable) EC	
ADDRESS (City, State, and ZIP Code) Monterey, CA 93943-5000		7b ADDRESS (City, State, and ZIP Code) Monterey, CA 93943-5000	
NAME OF FUNDING/SPONSORING ORGANIZATION		9 PROCUREMENT INSTRUMENT IDENTIFICATION NUMBER	
ADDRESS (City, State, and ZIP Code)		10 SOURCE OF FUNDING NUMBERS	
		PROGRAM ELEMENT NO	PROJECT NO
		TASK NO	WORK UNIT ACCESSION NO.
1. TITLE (Include Security Classification) A COMPARISON OF HIGH-LATITUDE IONOSPHERIC PROPAGATION PREDICTIONS FROM ADVANCED PROPHET 4.0 WITH MEASURED DATA			
2. PERSONAL AUTHOR(S) IKAS, Stefanos S.			
3a. TYPE OF REPORT Master's Thesis		13b. TIME COVERED FROM _____ TO _____	14. DATE OF REPORT (Year, Month, Day) 1990 December
15. PAGE COUNT 92			
5. SUPPLEMENTARY NOTATION The views expressed in this thesis are those of the author and do not reflect the official policy or position of the Department of Defense or the US Government.			
7. COSATI CODES		18. SUBJECT TERMS (Continue on reverse if necessary and identify by block number)	
FIELD	GROUP	SUB-GROUP	
		High Frequency (HF); Ionospheric Propagation; High-Latitude Regions	
9. ABSTRACT (Continue on reverse if necessary and identify by block number)			
<p>Progress in computers during the past two decades has sparked the development of many useful high frequency (HF) ionospheric propagation prediction codes. The high-latitude (polar) ionosphere still remains as the most difficult propagation region to predict.</p> <p>A "Noncentric" database of collected high-latitude signal and noise measurements was obtained during 1988 and 1989 by the University of Leicester, U.K..</p> <p>The Advanced Prophet 4.0 HF Ionospheric Propagation Prediction Code was exercised and compared to a portion of the "Noncentric" database, for a transmitter at Clyde River, Canada and a receiver at Leicester, U.K.. The prophet predictions were better during winter months than during summer months. Overall, 70% of the signal strength data from Prophet 4.0 were between -20 dB and +20 dB error, compared to the measured data.</p>			
10. DISTRIBUTION/AVAILABILITY OF ABSTRACT <input checked="" type="checkbox"/> UNCLASSIFIED/UNLIMITED <input type="checkbox"/> SAME AS RPT <input type="checkbox"/> DTIC USERS		21. ABSTRACT SECURITY CLASSIFICATION UNCLASSIFIED	
22a. NAME OF RESPONSIBLE INDIVIDUAL Richard W. Adler		22b. TELEPHONE (Include Area Code) 408-646-2352	22c. OFFICE SYMBOL EC/Ab

Form 1473, JUN 86

Previous editions are obsolete

SECURITY CLASSIFICATION OF THIS PAGE

S/N 0102-LF-014-6603

UNCLASSIFIED

Approved for public release; distribution is unlimited

A Comparison of High-Latitude Ionospheric Propagation  
Predictions from Advanced PROPHET 4.0 with Measured Data

by

Stefanos S. Gikas  
Lieutenant, Hellenic Navy  
B.S., Hellenic Naval Academy, 1981

Submitted in partial fulfillment of the  
requirements of degree of

MASTER OF SCIENCE IN ELECTRICAL ENGINEERING

from the

NAVAL POSTGRADUATE SCHOOL  
December 1990

Author:



Stefanos S. Gikas

Approved by:



Richard W. Adler, Thesis Advisor



Steve Jauregui, Second Reader



Michael A. Morgan, Chairman  
Department of Electrical and Computer Engineering

## ABSTRACT

Progress in computers during the past two decades has sparked the development of many useful high frequency (HF) ionospheric propagation prediction codes. The high-latitude (polar) ionosphere still remains as the most difficult propagation region to predict.

A "Noncentric" database of collected high-latitude signal and noise measurements was obtained during 1988 and 1989 by the University of Leicester, U.K..

The Advanced Prophet 4.0 HF Ionospheric Propagation Prediction Code was exercised and compared to a portion of the "Noncentric" database, for a transmitter at Clyde River, Canada and a receiver at Leicester, U.K. The Prophet predictions were better during winter months than during summer months. Overall, 70% of the signal strength data from Prophet 4.0 were between -20 dB and +20 dB error, compared to the measured data.



iii

Accession For	
NTIS GRA&I	<input checked="" type="checkbox"/>
DTIC TAB	<input type="checkbox"/>
Unannounced	<input type="checkbox"/>
Justification	
By	
Distribution	
Availability Codes	
Dist	Special
A-1	

## TABLE OF CONTENTS

I.	INTRODUCTION.....	1
A.	OVERVIEW.....	1
B.	PROPAGATION MODELS.....	2
C.	THE CLYDE RIVER-LEICESTER SHORTWAVE LINK.....	3
D.	ANALYSIS OF PREDICTIONS.....	5
II.	DESCRIPTION OF ADVANCED PROPHET 4.0.....	6
III.	THE SLOPING-VEE ANTENNA MODEL.....	9
A.	INTRODUCTION.....	9
B.	THE MODELING PROCESS.....	10
C.	ANALYSIS OF THE RESULTS.....	14
IV.	COMPARISON OF PROPHET'S PREDICTIONS WITH MEASUREMENTS.....	17
A.	THE "NONCENTRIC" DATABASE.....	17
B.	PROPHET'S SCENARIO PARAMETERS.....	21
C.	ANALYSIS OF PREDICTIONS.....	22
1.	Assumptions.....	22
2.	The Winter 1989 Campaign.....	24
3.	The Summer 1988 Campaign.....	28
4.	Seasonal Variation of Predictions.....	28
5.	Macroscopic View of All Data Analysed.....	32
V.	CONCLUSIONS AND RECOMMENDATIONS.....	41

APPENDIX A	ELEMENTS OF SHORTWAVE THEORY.....	43
APPENDIX B	RADIATION PATTERNS OF THE SLOPING-VEE ANTENNA...	73
APPENDIX C	NEC DATA SET FOR THE SLOPING-VEE ANTENNA.....	74
LIST OF REFERENCES.....		75
INITIAL DISTRIBUTION LIST.....		77

## LIST OF FIGURES

Figure 1. The geographical location of the Leicester-Clyde River shortwave link. . . . .	4
Figure 2. Configuration of the sloping-vee antenna . .	11
Figure 3. The elevation and azimuth radiation patterns of the sloping-vee antenna at 3 MHz. . . . .	12
Figure 4. Elevation and azimuth radiation patterns of the sloping-vee antenna at 8 MHz. . . . .	13
Figure 5. Elevation and azimuth radiation patterns of the sloping-vee antenna at 20 MHz. . . . .	15
Figure 6. Variation of the real and imaginary part of the input impedance of the sloping-vee antenna with the frequency. . . . .	16
Figure 7. Frequency spectrum of a CW signal; (a) with noise, (b) with the noise removed [From Ref. 4]. . . . .	19
Figure 8. The frequency spectrum of the call sign portion of the transmission [Ref. 4]. . . . .	20
Figure 9. Propagating modes in the Leicester-Clyde River shortwave link, at 10 MHz, on 8-9- 1988 at 21.01 U.T.. . . . .	23
Figure 10. Frequency distribution of the prediction error, $e$ , for the winter 1989 campaign. . . . .	25

Figure 11. Frequency distribution of prediction error, $e'$ , (mean=0), for the winter 1989 campaign. . . . .	26
Figure 12. Cumulative distribution of the absolute value of Prophet prediction errors for the winter 1989 campaign. . . . .	27
Figure 13. Frequency distribution of the Prophet predicted error, $e$ , for the summer 1988 campaign. . . . .	29
Figure 14. Frequency distribution of the Prophet prediction error, $e'$ , for the summer 1988 campaign. . . . .	30
Figure 15. Cumulative distribution of the absolute value of Prophet prediction errors, $e$ , and $e'$ , (summer 1988). . . . .	31
Figure 16. Frequency distribution of the Prophet prediction error, $e$ , for the two campaigns. . . . .	33
Figure 17. Frequency distribution of the Prophet prediction error, $e'$ , for the two campaigns. . . . .	34
Figure 18. Cumulative distribution of the absolute value of the prediction error, $e$ , for the two campaigns. . . . .	35



Figure 19. Cumulative distribution of the absolute value of the Prophet prediction error, $e'$ , for the two campaigns. . . . .	36
Figure 20. Frequency distribution of the Prophet prediction error, $e$ , for all the data analyzed. . . . .	38
Figure 21. Frequency distribution of the Prophet prediction error, $e'$ , for all the data analyzed. . . . .	39
Figure 22. Cumulative distribution of the absolute value of Prophet prediction errors, $e$ , and $e'$ . . . . .	40
Figure 23. Diurnal variation of electron density and the formation of ionospheric layers. From [Ref. 12: p. 21]. . . . .	47
Figure 24. The true reflection height $h$ , and the virtual height $h'$ . From [Ref. 11: p. 63]. . . . .	50
Figure 25. A typical ionogram. The superscripts $o$ and $x$ refer to ordinary and extraordinary waves. From [Ref.10: p. 79]. . . . .	51
Figure 26. The MUF factor $MUF_f$ , versus range $d$ . The layers F2a and F2b represent winter day and night respectively, and F2c a summer day or night. From [Ref. 10: p. 82]. . . . .	53

Figure 27. Variation of the critical frequency $f_o$ , with the sunspot number. From [Ref. 12: p. 23]. . . . .	54
Figure 28. Monthly mean of the noon critical frequencies observed at Slough during the last sunspot cycle 1970-1981. From [Ref. 11: p. 68]. . . . .	55
Figure 29. Diurnal variation of monthly median $f_oF_2$ observed at Slough. From [Ref. 11: p. 73]. . . . .	56
Figure 30. Ray paths against launch angles for a fixed frequency. From [Ref. 11: p. 62]. . . .	57
Figure 31. Various propagation modes for multi-hop links. From [Ref. 12: p. 41]. . . . .	58
Figure 32. Seasonal distribution of very large geomagnetic storms from 1932 to 1984. From [Ref. 16: p. 5-32]. . . . .	65
Figure 33. The probability that a given level of absorption will be exceeded at an area of maximum absorption. From [Ref. 17: p. 1357]. . . . .	68
Figure 34. Association of PCA with the level of solar activity for the period 1949-1961. From [Ref. 13: p. 279]. . . . .	70

## **I. INTRODUCTION**

### **A. OVERVIEW**

High frequency (HF) (2-30 MHz) electromagnetic waves have been, and still are, extensively used to meet the plethora of military and civilian communications requirements.

Although in the 70's HF fell into disfavor because communication satellites emerged as an alternative to HF, in the 80's HF regained its vital role as a flexible, inexpensive, and resilient communications capability. HF offers low cost equipment, low power requirements, and adequate bandwidths.

From the military point of view, reliable communications between the decision making centers and units in the air, sea, and land are essential.

For large military organizations like N.A.T.O. long-distance communications are extremely important since the area of operations extends from the high Arctic to the equator and from the Mediterranean Sea to the Pacific Ocean.

Long-distance communications at HF is achieved via skywave propagation. Skywaves are launched at a range of angles and travel upwards to be reflected from the ionosphere. The ionosphere varies diurnally, seasonally, and with solar

activity in observable patterns, but is still quite unpredictable and variable for short-term applications.

Of particular interest is the high-latitude ionosphere which is controlled to a great extent by the earth's magnetic field. The variability of high-latitude signals during disturbances can be attributed to the variability in shape and density of high-latitude ionosphere.

For many years high-latitude HF propagation had been an enigma primarily due to insufficient analyzable data. During the last decade, however, many experiments have helped to explain and permitted analysis of some high-latitude ionospheric phenomena.

In Appendix A, the basic concepts of skywave propagation and the effects of the high-latitude ionosphere on HF communications are briefly presented.

## **B. PROPAGATION MODELS**

The remarkable progress in computer systems over the past two decades has made it practical to develop models of the ionosphere with the objective of making propagation predictions.

There are two kinds of ionospheric models, empirical and mathematical. Empirical models are based on data compilation; conversely, mathematical models are based on theoretical physical descriptions of the ionosphere.

Propagation models are constructed by adding ray-tracing routines, attenuation models, and noise models to an ionospheric model in order to predict the characteristics of propagation (field strength, maximum usable frequency, propagation mode etc.). The ionospheric model depends on an empirical database and the propagation models, therefore, omit day-to-day variability and tend to be less accurate in equatorial and polar regions.

A large number of prediction codes are available such as: PROPHET, IONCAP, WOMAP, AMBCOM, HFMUFES, APPLAB, CCIR252 etc. This thesis is concerned with the Advanced PROPHET 4.0 [1] propagation prediction code and the accuracy of its predictions for polar paths. In Chapter II, the capabilities of Advanced PROPHET are described.

### **C. THE CLYDE RIVER-LEICESTER SHORTWAVE LINK**

Recently, scientists from the University of Leicester, U.K., conducted a series of signal and noise measurements on a shortwave link from Clyde River (CANADA) to Leicester, U.K., (Figure 1). A "Noncentric" database thus created may be the largest collection of polar signal and noise data to date. The "Noncentric" term is used only for identification of data source, since these measurements were a subset of data from Project "Noncentric".

The "Noncentric" database was not constructed for the evaluation of PC-based propagation prediction codes. It is not

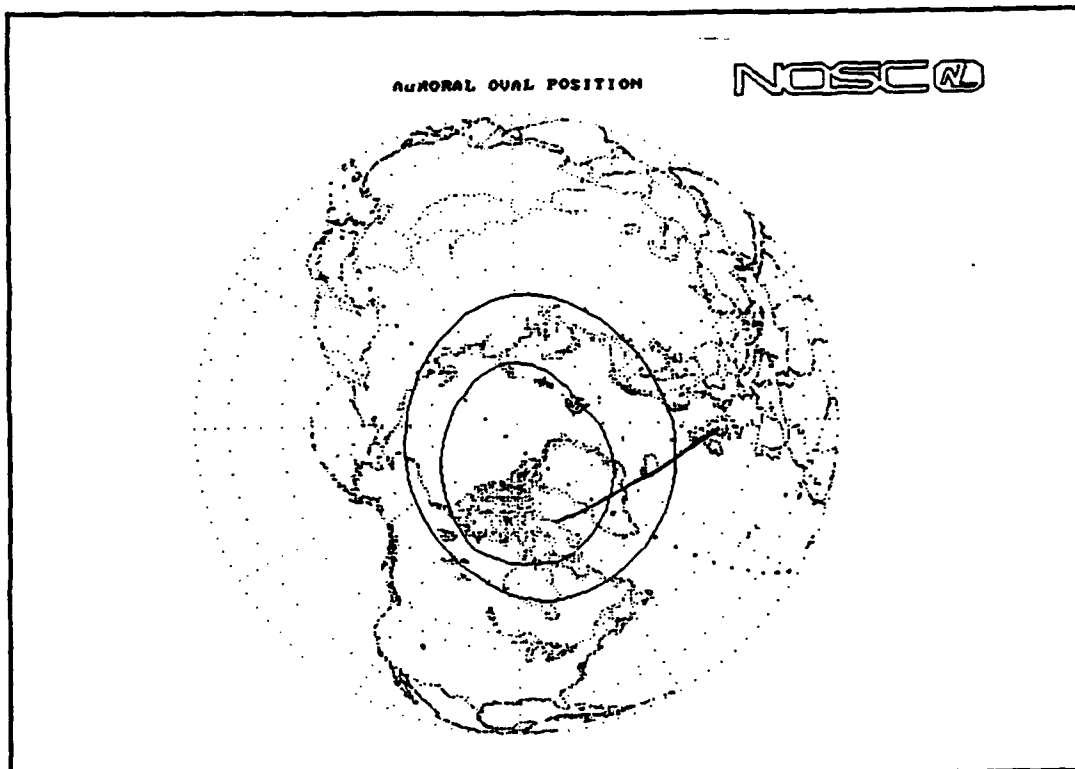


**Figure 1. The geographical location of the Leicester-Clyde River shortwave link.**

applicable for incoming field strength comparisons, but for signal-to-noise ratio comparisons at receiver input terminals. The reasons for the database not providing incoming field strength are twofold: First, the antenna radiation characteristics at the transmitter and at the receiver were not established and second, the RF signal distribution system characteristics between the receive antenna terminals and the input to the receiver were never determined, and if they had been, it is highly probable that they would have varied substantially with time.

The "Noncentric" database covers 1988 and 1989 but only data of "site O" (summer 1988 and winter 1989) were available and utilized in this study.

The receiver antenna, located at Leicester, is a sloping-vee antenna which consists of two terminated sloping wire antennas with a  $90^\circ$  interior angle. Chapter III describes how the antenna was simulated and analyzed using the Numerical Electromagnetics Code (NEC) [2]. The calculated radiation patterns were installed in Advanced PROPHET for the receiving site.

The transmitter antennas, located at Clyde River, were a loaded vertical monopole for the winter 1989 campaign, and a "Butternut" trap-vertical monopole for the summer 1988 campaign. Their radiation patterns were obtained from Ref. 3 and were also installed in Advanced PROPHET for the transmitter site.

#### D. ANALYSIS OF PREDICTIONS

In Chapter IV, Advanced PROPHET's predictions of signal-to-noise ratio were compared with the University of Leicester's measured signal-to-noise data, by computing the prediction error,  $e$ , of each campaign, where  $e = (S/N)_{\text{PROF}} - (S/N)_{\text{LEIC}}$ . Finally, the predictions of the two campaigns were compared to show the seasonal variation.

## II. DESCRIPTION OF ADVANCED PROPHET 4.0

Advanced PROPHET 4.0, developed at NOSC in 1989, is a successor to Advanced PROPHET 3.2. Advanced PROPHET is a collection of computer simulation models designed to support tactical use of the HF band.

It can determine the existence of an HF skywave channel between a transmitter and a receiver located anywhere in the world [1]. The modeling approach in PROPHET uses empirical models which have been fitted to experimental data. That is, the models were derived from an extensive data set of measurements taken from various sources rather than by applying a detailed physical model.

Advanced PROPHET consists of several computer algorithms capable of solving a great variety of HF problems. The standard PROPHET skywave calculation method involves three important algorithms: "MUFLUF", "MUF85" and "DAMBLT".

The main objective of any HF prediction program is to determine accurately the skywave propagation bandwidth between the LUF and the MUF for any set of conditions. This is achieved by the "MUFLUF" algorithm which computes the path geometry between the transmitter and receiver. The MUF is estimated at the path midpoint using the "MUF85" algorithm. "MUF85" (also called MINIMUF) is a curve fit of first order



exponential functions to a large database of HF sounder measurements. It provides a good approximation of MUF between any two geographical points. The "classical MUF" is scaled by interpolating a data table to determine the operational MUF and also the frequency of optimum transmission (FOT). The FOT is defined as a frequency with 90% reliability. A comparable algorithm has been developed to estimate the LUF. The LUF is determined in part by the solar insolation along a great circle path between two points. The algorithm for the estimation of LUF has been improved in version 4.0.

Once the operational MUF and LUF have been established, the signal strength is determined by the "DAMBLT" algorithm. Constructed by T. Damboldt of the German Bundesposte, "DAMBLT" is an empirical fit of signal strength. This empirical fit depends upon the ratio of the operating frequency to the MUF, the ratio of the LUF to the frequency, and the path length. PROPHET 4.0 is also equipped with an improved algorithm for field strength predictions in polar regions.

The "MUFLUF", "MUF85", and "DAMBLT" models comprise the basis for PROPHET's predictions. A number of other empirical models offer more sophisticated capabilities: (1) the ray-tracing program that computes the propagation modes and the actual path traversed by an HF signal between the transmitter and receiver; (2) an empirical model that locates the auroral oval with mapping options; and (3) an empirical model for the

scintillation of downlink signals from a geostationary satellite.

A model for the expected noise for various environments includes contributions from atmospheric, man-made, and galactic noise sources. Influences by jammer sites are also included.

A large variety of input parameters form the different scenarios of HF problems. Parameters of great importance include: (1) antenna radiation patterns, (2) modulation parameters such as modulation type, bandwidth, and required signal-to-noise ratio, (3) geophysical parameters such as solar sunspot activity, magnetic and ionospheric storms, and (4) environmental parameters such as the type of terrain and cover for groundwave calculations. (Groundwave calculations with PROPHET are not recommended though, until existing errors are corrected).

Advanced PROPHET products are utilized to guide operators of HF communication equipment to improve the effectiveness of the HF channel, and to reduce the probability of intercept and the vulnerability to a jammer threat.

### III. THE SLOPING-VEE ANTENNA MODEL

#### A. INTRODUCTION

Long-wire antennas are usually several wavelengths long and are often used in the HF band (2 to 30 MHz). The best known types are: the horizontal-vee antenna, the horizontal-rhombic antenna, the sloping-rhombic antenna, the vertical-vee antenna, the vertical inverted-vee antenna, the sloping-vee antenna, and the single horizontal wire antenna.

Long-wire antennas may be characterized as resonant antennas (standing-wave) and traveling-wave antennas. In the case of resonant antennas, the current on the wire is a standing wave with sinusoidal variation. Resonant antennas usually operate satisfactorily only at a particular frequency and harmonics of this frequency. The input impedance is very dependent on frequency, resulting in narrow-band operation.

For the traveling-wave case, a long-wire antenna is operated as a nonresonant antenna by virtue of termination of the far end of the wires using a load resistor which matches the characteristic impedance of the antenna when it is viewed as a transmission line. Traveling-wave antennas have wide bandwidth and present a useable impedance over a wide range of frequencies.

## B. THE MODELING PROCESS

The sloping-vee antenna, used at the University of Leicester U.K. as a receiving antenna in the Clyde River-Leicester link, consists of two sloping straight wire antennas arranged with an interior angle of  $90^\circ$ . Figure 2 illustrates the configuration and dimensions of the sloping-vee antenna. The two long arms of the antenna are terminated in 600 Ohm loads and a 1 meter ground stake, producing traveling-wave operation.

The sloping-vee was modeled via NEC [3]. NEC was developed at the Lawrence Livermore Laboratory at Livermore California and is a user-oriented computer code for analysis of the electromagnetic response of antennas and other metal structures. It is a versatile code with wire antenna modeling capabilities that, include transmission lines, networks, loading and ground effects.

A typical input data set is in Appendix C. Modeling a wire structure in NEC involves both geometrical and electrical factors. The main electrical consideration is the wire segment length relative to the wavelength.

Forty-one segments were used for each of the 100 m long arms of the sloping-vee antenna. For the frequency band of interest, 3-20 MHz ( $15\text{m} < \lambda < 100\text{m}$ ), the length of each segment varies from  $0.02\lambda$  to  $0.16\lambda$  over the band. These limits are within NEC modeling guidelines. The segment size determines the resolution for the current on the model since current is

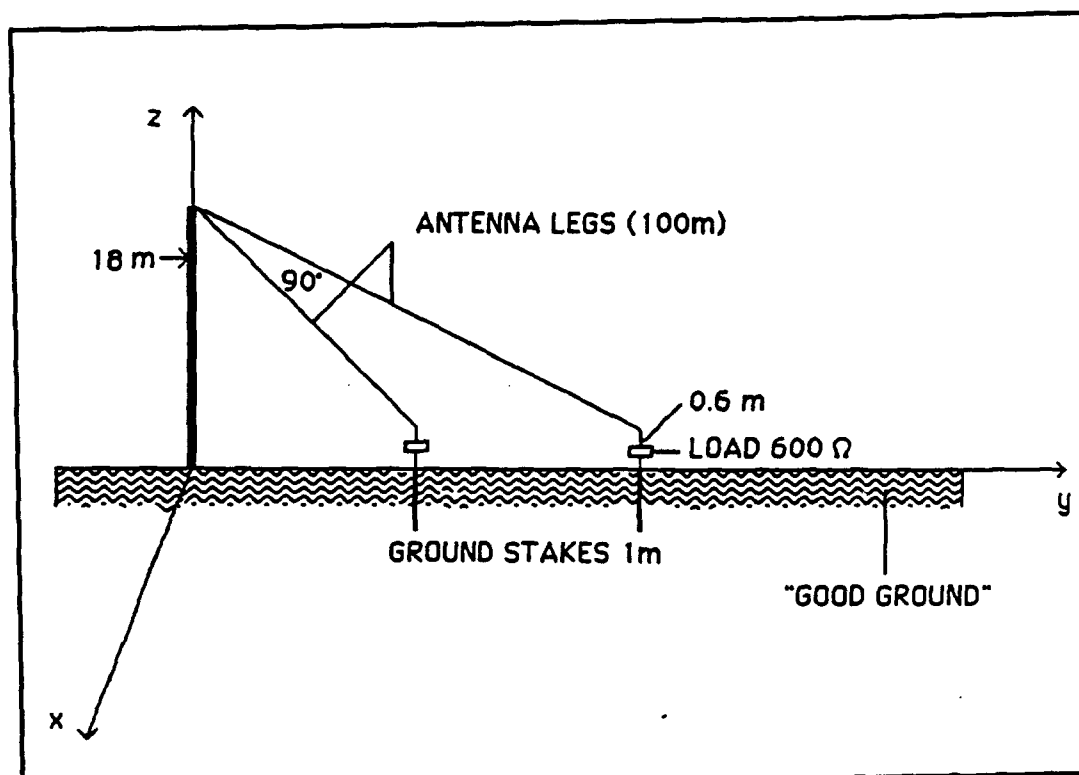


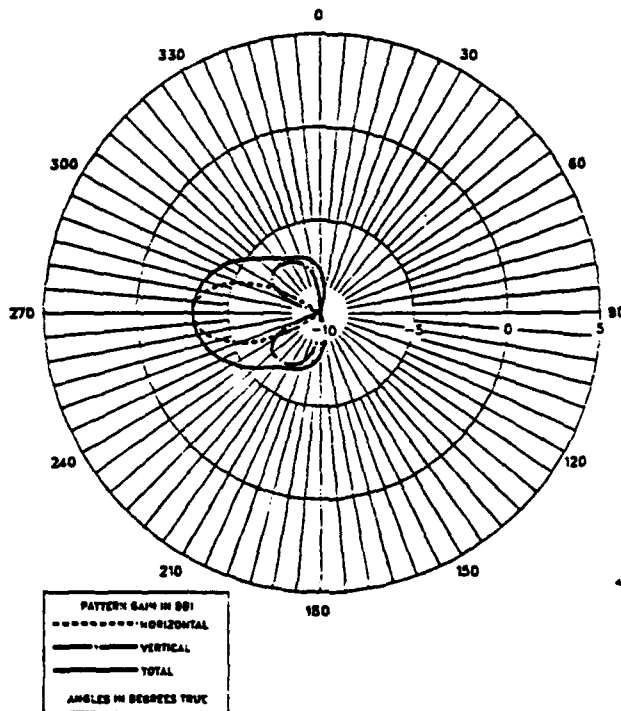
Figure 2. Configuration of the sloping-vee antenna

computed at the center of each segment.

Parameters for "good ground" ( $\sigma=30$ ,  $\epsilon=0.01$ ) were used to simulate the terrain of the sloping-vee. Due to the presence of finite ground, the Sommerfield/Norton method was utilized for accurate results.

Two feed points and the voltage source option were used to specify the excitation of the structure. The two feed points, seen in Figure 2, are located 1.2 m from the beginning of each long arm.

SLOPING VEE ANTENNA, ANGLE VEE 90 DEGREES, FREQ. 3 MHZ,  
ELEV. ANGLE = 45 DEG. (GOOD GROUND).



SLOPING VEE ANTENNA, ANGLE VEE 90 DEGREES, FREQ. 3 MHZ,  
PHI = 90 DEG. (GOOD GROUND).

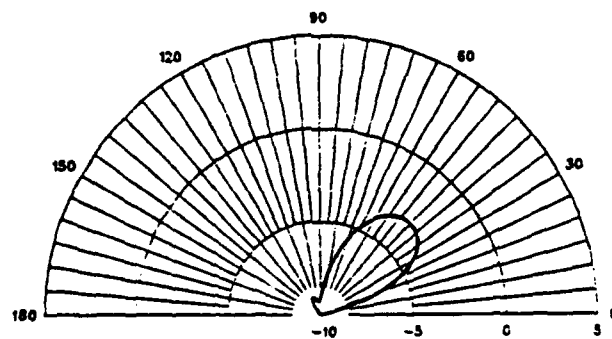
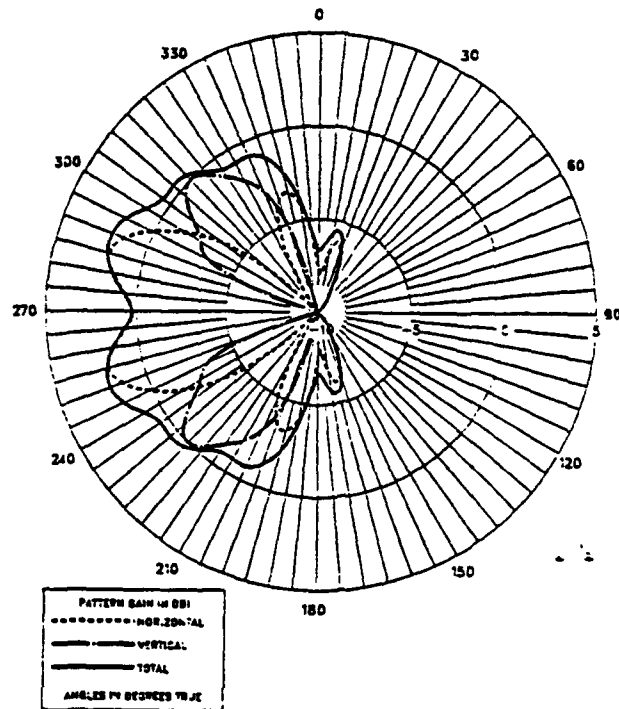


**Figure 3. The elevation and azimuth radiation patterns of the sloping-vee antenna at 3 MHz.**

SLOPING VEE ANTENNA, ANGLE VEE 90 DEGREES, FREQ. 8 MHZ,  
ELEV. ANGLE = 22 DEG. (GOOD GROUND).



SLOPING VEE ANTENNA, ANGLE VEE 90 DEGREES, FREQ. 8 MHZ,  
PHI = 90 DEG. (GOOD GROUND).

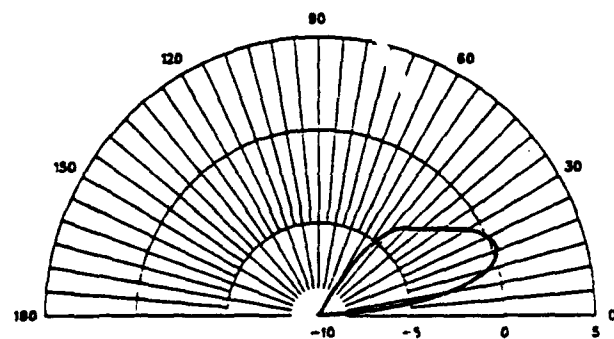


**Figure 4. Elevation and azimuth radiation patterns of the sloping-vee antenna at 8 MHz.**

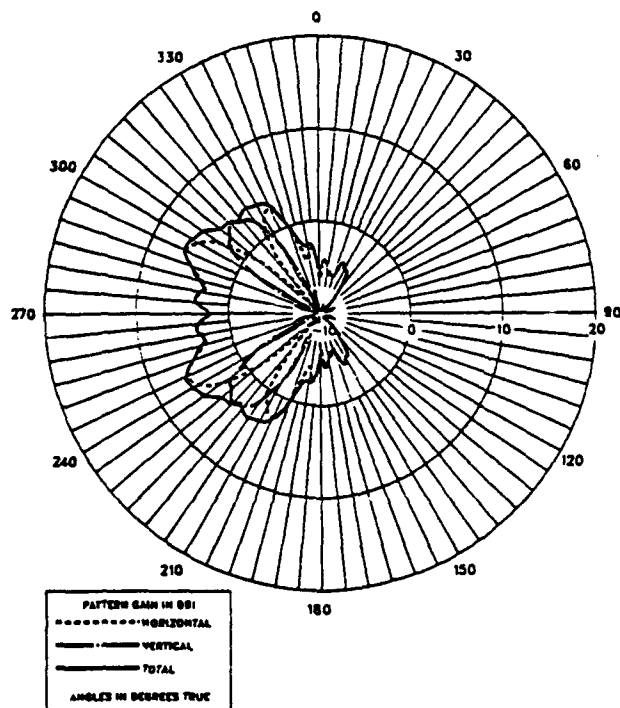
### C. ANALYSIS OF THE RESULTS

Figures 3, 4, and 5, contain the elevation and azimuth radiation patterns of the sloping-vee for 3, 8, and 20 MHz. The patterns are as expected from antenna theory.

Finally, Figure 6 illustrates the variation of the input impedance over the band. Note that the variation is rather small, and the values of input impedance are within the expected range.



SLOPING VEE ANTENNA, ANGLE VEE 90 DEGREES, FREQ. 20 MHZ,  
ELEV. ANGLE = 11 DEG. (GOOD GROUND).



SLOPING VEE ANTENNA, ANGLE VEE 90 DEGREES, FREQ. 20 MHZ,  
PHI = 90 DEG. (GOOD GROUND).

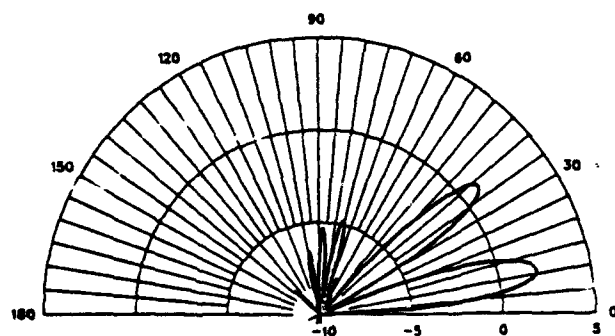


**Figure 5. Elevation and azimuth radiation patterns of the sloping-vee antenna at 20 MHz.**

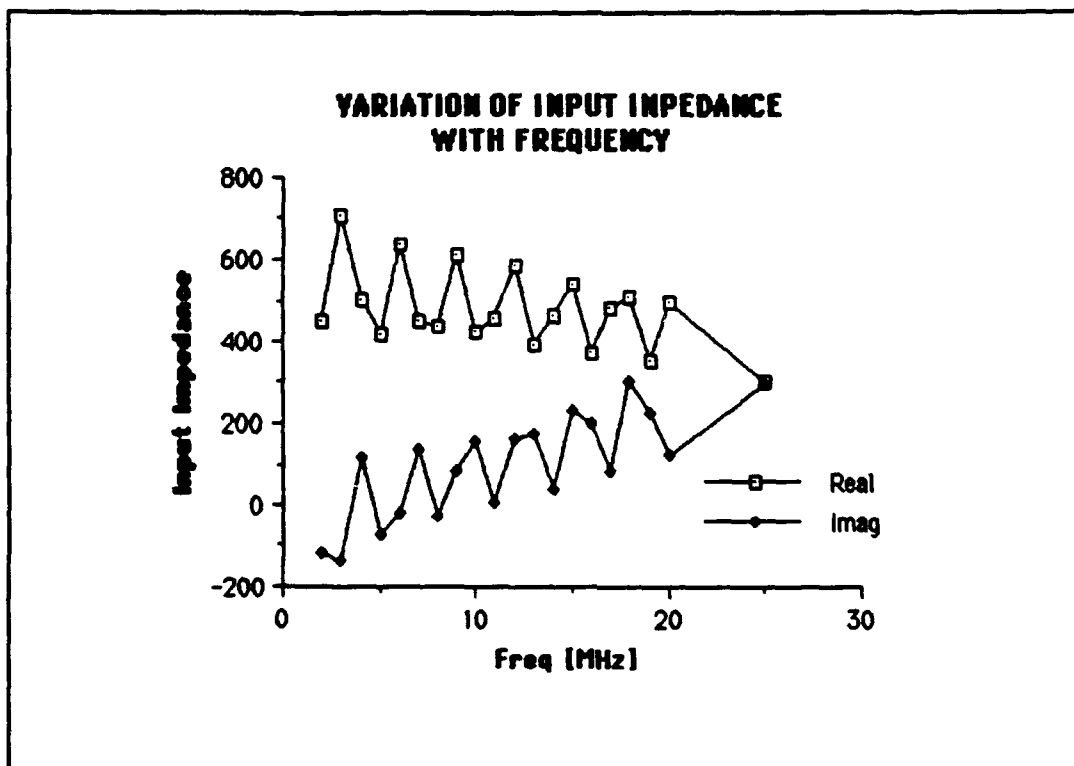


**Figure 6.** Variation of the real and imaginary part of the input impedance of the sloping-vee antenna with the frequency.

#### **IV. COMPARISON OF PROPHET'S PREDICTIONS WITH MEASUREMENTS**

##### **A. THE "NONCENTRIC" DATABASE**

The "Noncentric" database developed at the University of Leicester, U.K., consists of more than 80,000 signal and noise level data covering the two-year period of 1988-1989, for the Clyde River-Leicester path.

The data was first characterized by "campaigns". The two-year period was divided into twelve campaigns of approximately 25 days each from two consecutive months. The winter 1989 campaign, for example, consists of data obtained during the time period from 1-17-89 to 2-12-89 (25 days); and, similarly, the summer 1988 campaign consists of data obtained from 7-17-88 to 8-12-88 (also 25 days).

In order to speed-up the analysis of "Noncentric" data, two tests were developed [4] to detect the presence of the "Noncentric" signal. These are the Spread-Index test and the Call-Sign test.

The incoming signals at the receiver were processed using a 1,000 point fast Fourier transform (FFT) to calculate the doppler spreading of the received signal.

The Spread-Index test is based on ionospherically induced doppler spreading of a CW transmission. The spectrum of the received signal is normalized by setting the peak amplitude to

unity. The entire spectrum interval of the CW transmission is 50 Hz (from -25 Hz to +25 Hz) as can be seen in Figure 7a. The mean noise level of the first quarter of the spectrum (-25 Hz to -12.5 Hz) is assumed to represent the mean noise level of the whole spectrum. Thus, it is subtracted to yield a spectrum as depicted in Figure 7b. The Spread-Index is the area under the remaining signal which is proportional to the doppler spreading of the signal. The Spread-Index, in conjunction with the signal level measurements, provides the first recognition test as follows: if the Spread-Index is large the received signal passes the test, but, if the Spread- Index is small, the signal passes the test only if its signal level is high.

The Call-Sign test is based on the recognition of the call sign, CZB, transmitted three times in each two-minute sequence. A typical call-sign spectrum is illustrated in Figure 8. The signal recognition routine searches within the frequency interval from -5 Hz to +20 Hz in order to find a pattern similar to that of Figure 8 (a main signal peak with two side peaks). If this pattern is found, the signal passes the Call-Sign test.

The data, after undergoing the two recognition tests, were categorized into the following groups:

- (1) Signals passing both tests are identified as group SIG.
- (2) Signals failing both tests are identified as group NOS.

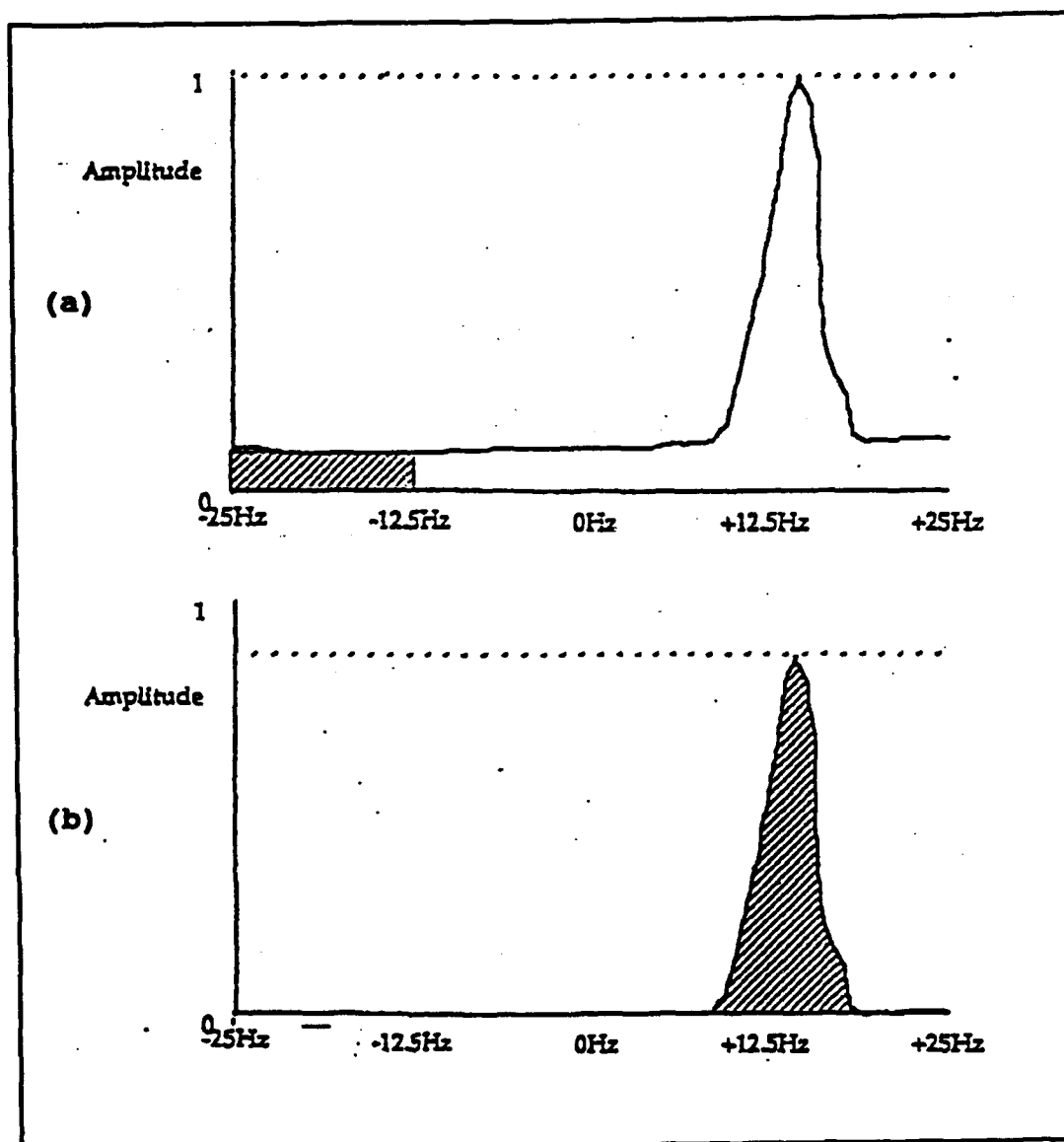


Figure 7. Frequency spectrum of a CW signal; (a) with noise, (b) with the noise removed [From Ref. 4].

- (3) Signals passing the Call-Sign test only are identified as group FCS.
- (4) Signals passing the Spread-Index test only are identified as group FSI.
- (5) Signals characterized as interference are identified as group INT.

The "Noncentric" data base is comprised of the sum of all the groups except that from the INT group (interference). Overall, however, the confidence in signals that passed both tests (SIG group) is much higher than that of the other groups. For this reason, in the present thesis, only the SIG

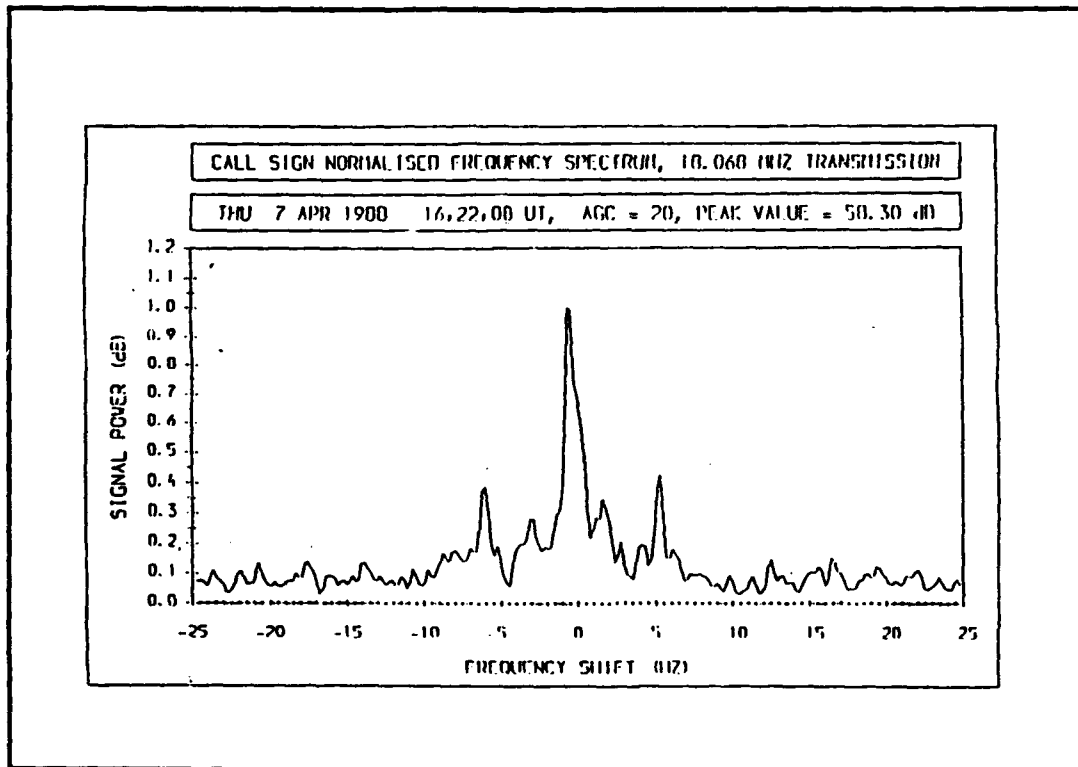


Figure 8. The frequency spectrum of the call sign portion of the transmission [Ref. 4].

groups of the winter 1989 and summer 1988 campaigns were considered.

## B. PROPHE'T'S SCENARIO PARAMETERS

In order to satisfactorily utilize the Advanced PROPHE'T's capabilities, an accurate creation of the appropriate scenario was necessary.

The antenna parameters were of great importance. Radiation patterns of three different antennas were used in Advanced PROPHE'T; a loaded vertical monopole, a "Butternut" trap-vertical monopole as transmitting antennas, and a sloping-vee antenna as a receive antenna.

In Appendix B, Advanced PROPHE'T's requirements for the three antennas are described. These patterns are listed in terms of the total gain (total = vertical + horizontal polarization) over the entire HF band (2-30 MHz).

Geomagnetic and solar scenario parameters were taken from Ref. [6],[7] and [8],[9] for the winter 1989 and summer 1988 campaigns, respectively. The daily average of the eight, three-hourly indices,  $K_p$ , was used as the input value for the planetary index  $K_p$ . Average values of sunspot number measured by two different agencies were used. The two agencies were the American Association of Variable Star Observers and the WDC-A for Solar-Terrestrial Physics.

The modulation type, CW with 50 Hz bandwidth, was also part of the Advanced Prophet scenario.

Finally, atmospheric noise and man-made noise were selected to simulate noise environments.

## C. ANALYSIS OF PREDICTIONS

### 1. Assumptions

In order to develop a quantitative measure of the prediction accuracy of Advanced Prophet, the model predictions of the signal-to-noise ratio,  $(S/N)_{PRO}$ , were compared with the empirical signal-to-noise ratio,  $(S/N)_{LEIC}$ , from the "Noncentric" database.

The statistical analysis of the prediction error,  $e = (S/N)_{PRO} - (S/N)_{LEIC}$ , was computed using the frequency distribution of the predicted errors and the cumulative distribution of the absolute value of the prediction errors.

Furthermore, a relative measure of the prediction accuracy was achieved by normalizing each set of prediction errors to zero statistical mean and recomputing the frequency distribution and the cumulative distribution of the prediction errors. In this case, the prediction error,  $e'$ , is given by  $e' = (S/N)_{PRO} - (S/N)_{LEIC} - E(e)$ , where  $E(e)$  is the mean of  $e$ .

The computation of signal-to-noise ratio, rather than the field strength, was necessary due to the limited characteristics of the "Noncentric" signal strength data, and the lack of information about the complexity of the receiver site.

The Clyde River-Leicester path is approximately 3,810 Km which implies the existence of multihop propagation modes. Figure 9 is an example of the ray-tracing routine of Advanced



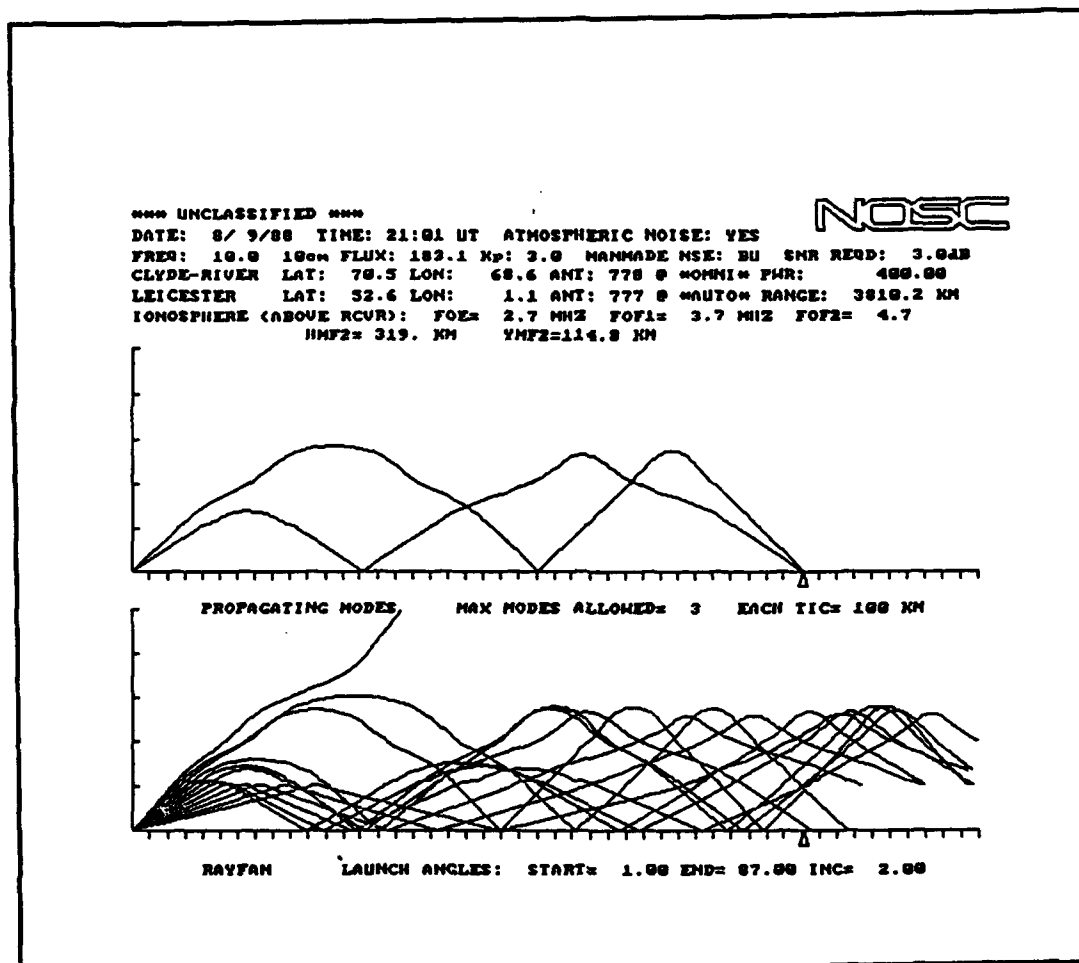


Figure 9. Propagating modes in the Leicester-Clyde River shortwave link, at 10 MHz, on 8-9-1988 at 21.01 U.T..

PROPHET which was utilized to yield the maximum number of propagating modes for 10 MHz on 8-9-1988 at 21.01 Universal Time.

The winter 1989 and summer 1988 campaigns involve 16 HF frequencies ranging from 3.185 to 23.169 MHz. Each frequency was transmitted at a pre-specified minute, hourly. For example, the 13.886 MHz frequency was transmitted at 22 minutes past the hour, the 10.195 MHz at 43 minutes past the

hour, the 20.3 MHz at 49 minutes past the hour and so on for every hour of the day and for every day of the campaign.

Since the prediction values of Advanced Prophet refer only to integer frequencies and at integer hours of the day, manual interpolation was conducted.

A total of 2,348 data points was used in the evaluation of Advanced Prophet 4.0 (approximately 60 % of the data from the SIG files of winter 1989 and summer 1988 campaigns).

## 2. The Winter 1989 Campaign

The SIG file of the winter 1989 campaign consists of 1,979 data and 13 frequencies. In the present analysis, 1,127 data were utilized for 6.8 MHz, 6.9 MHz, 9.9 MHz, 13.9 MHz, 17.5 MHz and 20.3 MHz. Advanced PROPHET predicted useable paths in 95.8% of the cases (1,080 out of 1,121 cases).

In Figure 10, the frequency distribution of the error,  $e$ , is depicted. The median error is -7.7 dB, and the standard deviation of the error is 14.7 dB. In Figure 11, the frequency distribution of the prediction error,  $e'$ , may be seen. The median error is now only 1.98 dB since the statistical mean is, by definition, zero.

Figure 12 illustrates the cumulative distribution of the absolute value of the error,  $e$ , (solid curve), and the cumulative distribution of the error,  $e'$ , (dashed curve). It is observed (for the case of  $e$ ) that 82% of Prophet's data are

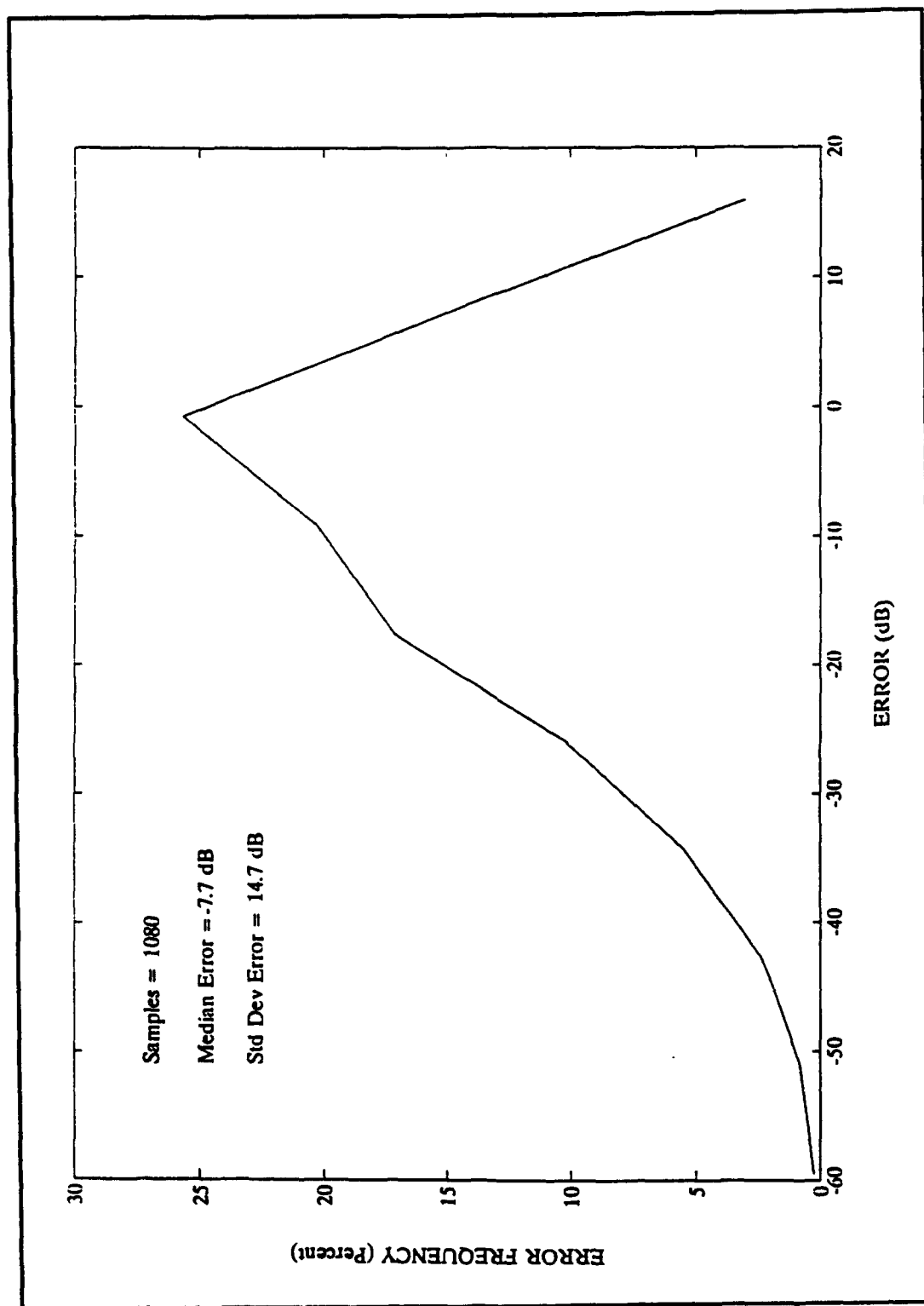


**Figure 10. Frequency distribution of the prediction error,  $e$ , for the winter 1989 campaign.**

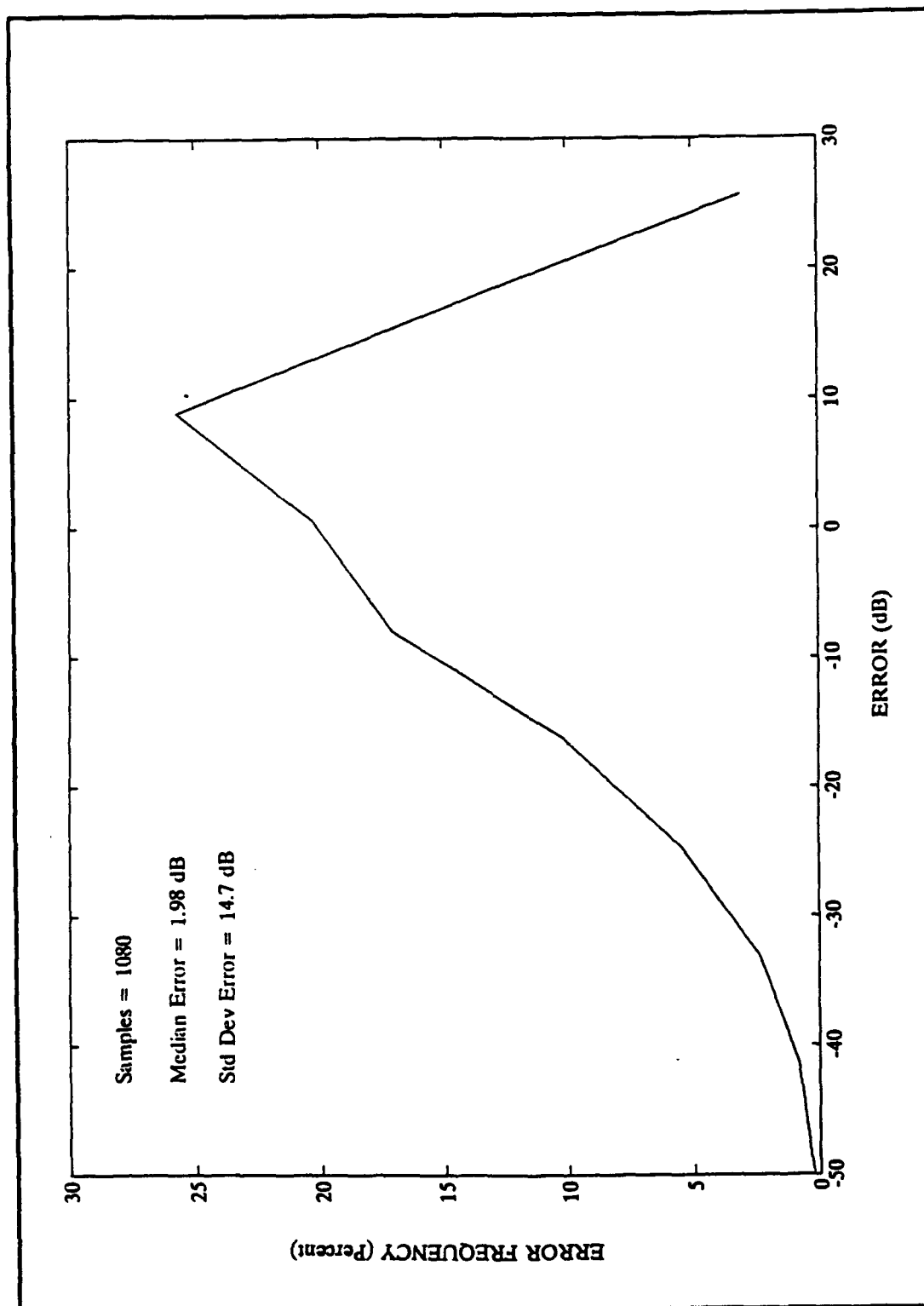
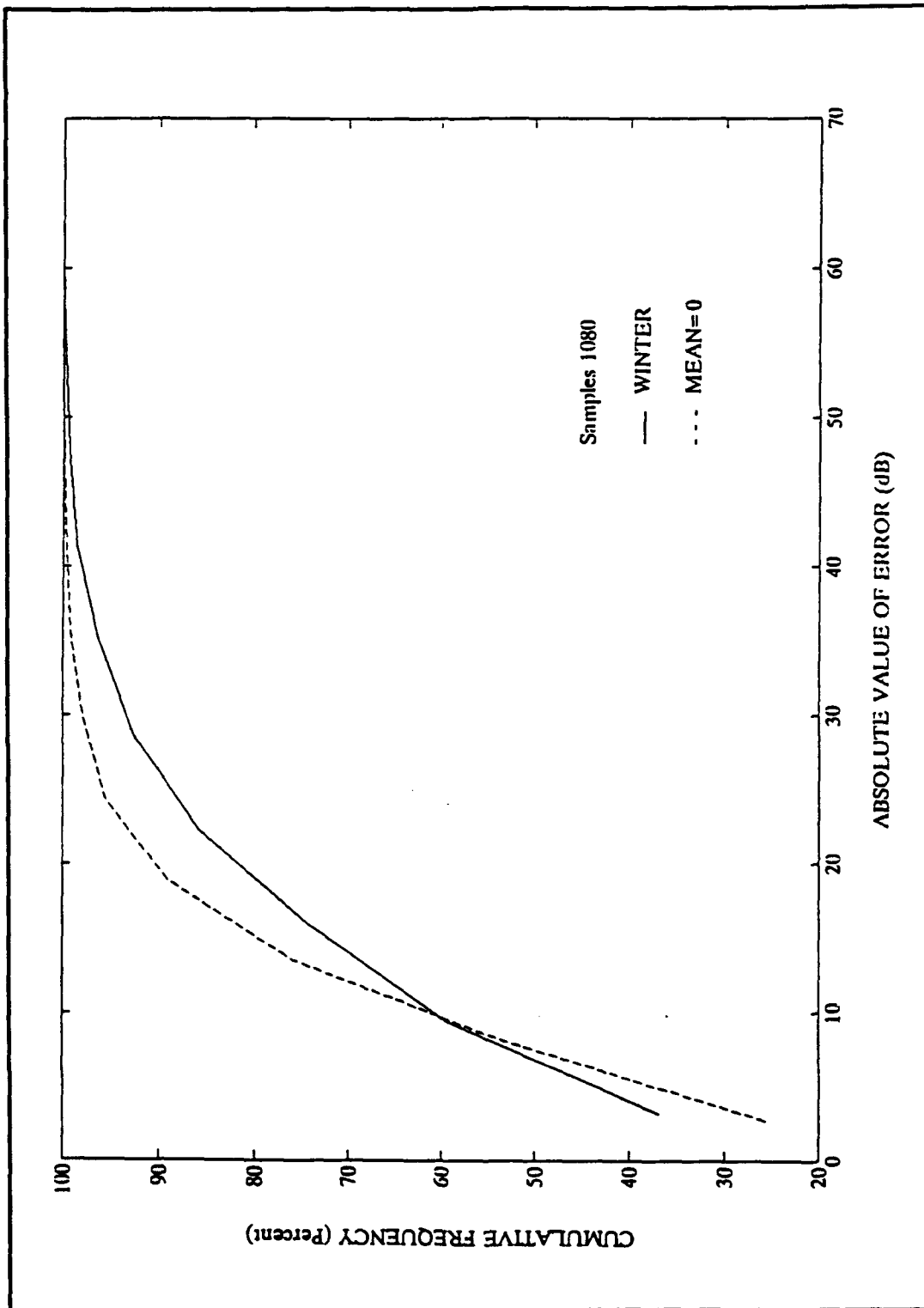


Figure 11. Frequency distribution of prediction error,  $e'$ , (mean=0), for the winter 1989 campaign.



**Figure 12. Cumulative distribution of the absolute value of Prophet prediction errors for the winter 1989 campaign.**

between -20 dB and +20 dB error while (for the case of  $e'$ ) 90.5% of Prophet's data are between -20 dB and +20 dB error.

### **3. The Summer 1988 Campaign**

The SIG file of the summer 1988 campaign consists of 1948 data points and 14 frequencies. Now, 1,221 data were utilized, involving the same frequencies as in the winter 1989 campaign plus the 10.1 MHz frequency. Advanced Prophet predicted useable paths in 1,080 out of 1,221 cases (88%).

Figures 13 and 14 show the frequency distribution of the predicted errors,  $e$ , and  $e'$ . The standard deviation of the predicted error is 14.28 dB, and the median error is -21 dB and -0.24 dB for the prediction errors,  $e$ , and  $e'$ , respectively.

Figure 15 illustrates the cumulative distribution of the absolute value of the prediction errors,  $e$ , and  $e'$ . For the case of  $e$  (solid curve), 56% of Prophet's data are between -20 dB and +20 dB error. On the other hand, for the case of  $e'$  (dashed curve), 88% of Prophet's data are between -20 dB and +20 dB error.

### **4. Seasonal Variation of Predictions**

In Figures 16 and 17, the frequency distribution of the prediction errors,  $e$ , and  $e'$  is shown respectively for the two campaigns. The peak value of the error frequency for the winter 1989 campaign is higher than the peak value of the

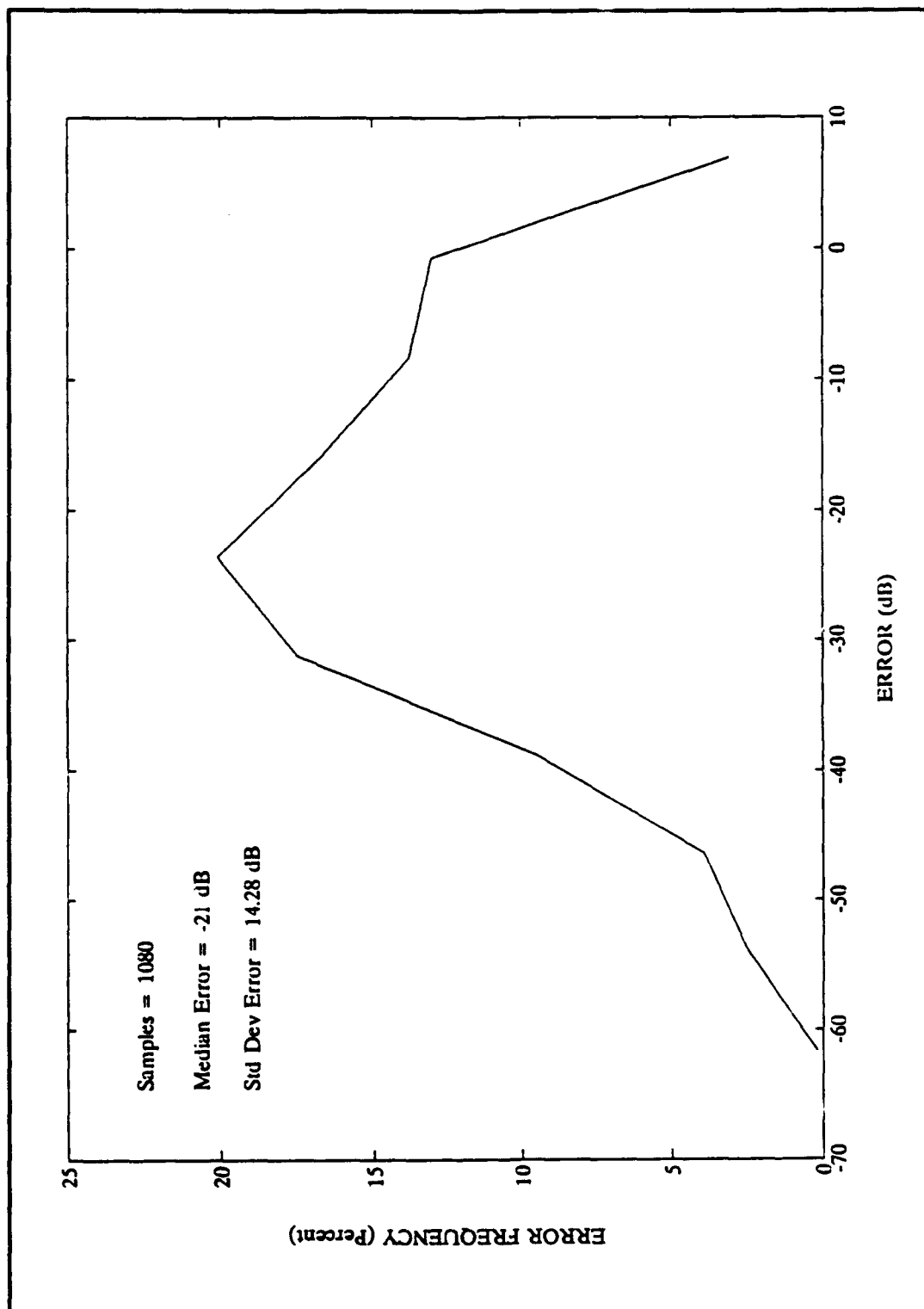


**Figure 13. Frequency distribution of the Prophet predicted error,  $e$ , for the summer 1988 campaign.**

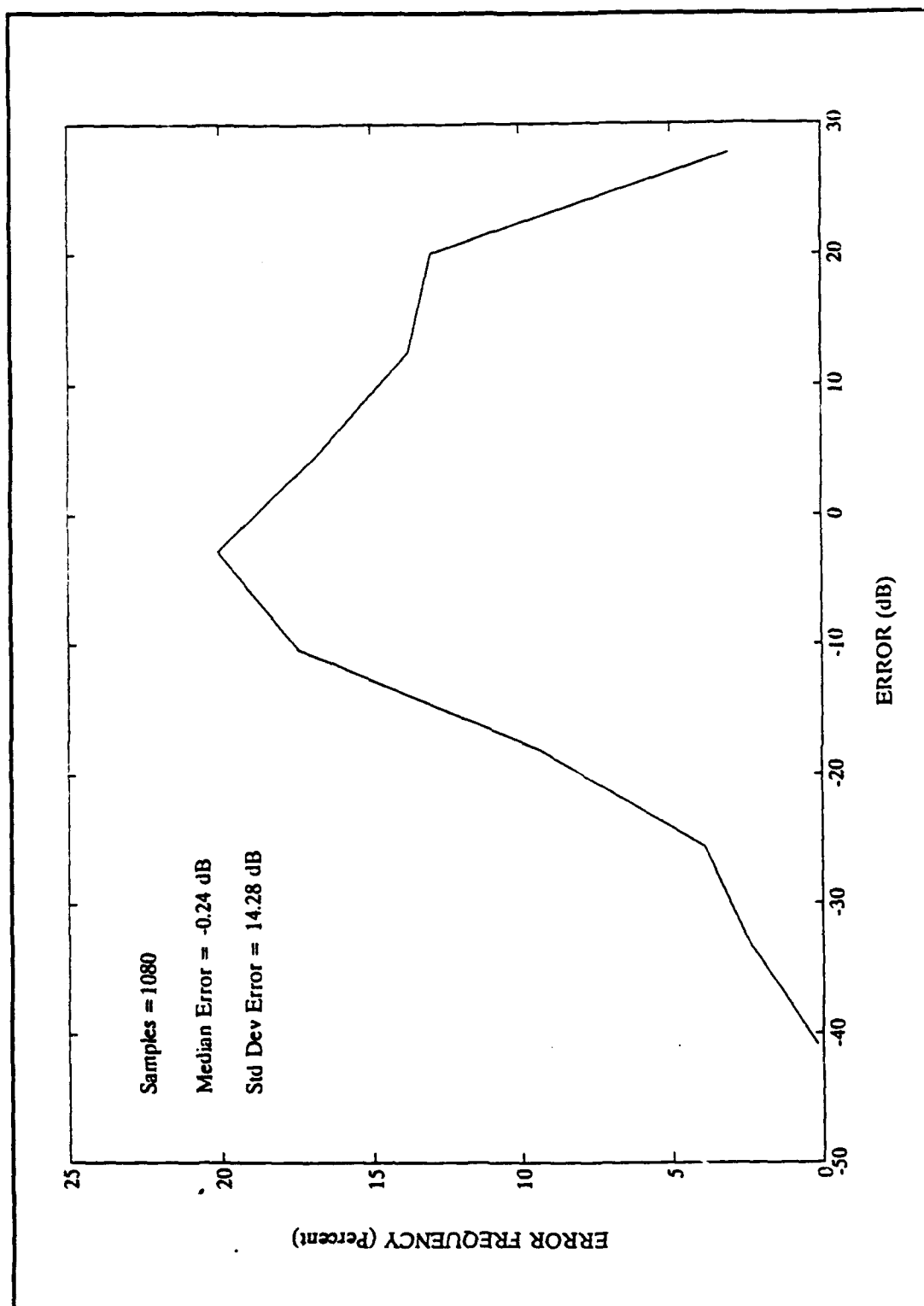


Figure 14. Frequency distribution of the Prophet prediction error,  $e'$ , for the summer 1988 campaign.



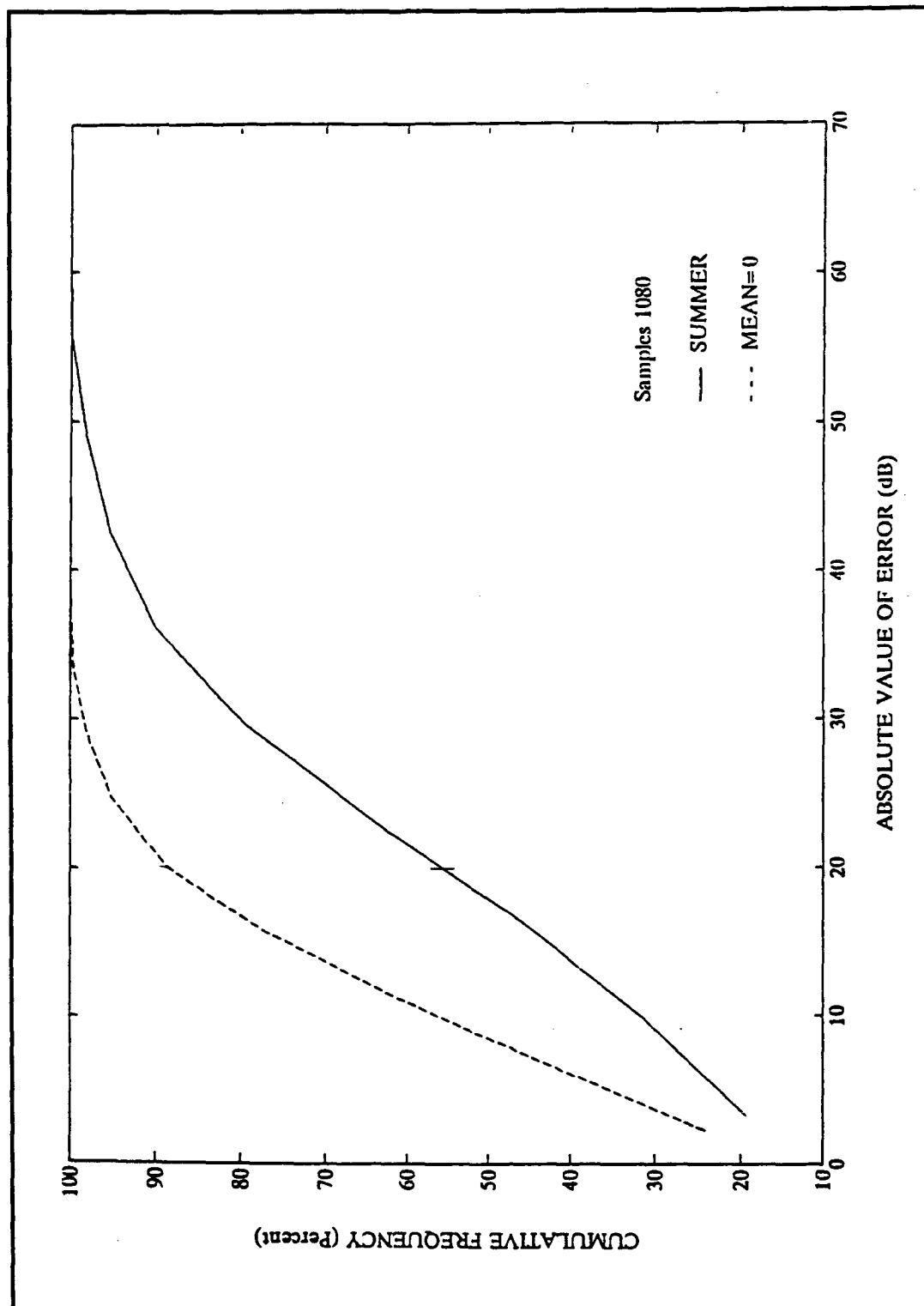


Figure 15. Cumulative distribution of the absolute value of Prophet prediction errors,  $e$ , and  $e'$ , (summer 1988).

summer 1988 campaign by 6% (26% and 20% respectively). In Figure 16, for prediction error,  $e$ , the error value corresponding to the peak value of error frequency, winter 1989 campaign, is -1 dB, and, summer 1988 campaign, -24 dB. Similarly, in Figure 17 for the prediction error,  $e'$ , the respective numbers are 8 dB for the winter 1989 campaign and -3 dB for the summer 1988 campaign.

Figure 18 shows the cumulative distribution of the absolute value of the prediction error,  $e$ , for the two campaigns. It is seen that 82% of the Prophet data of the winter 1989 campaign and only 56% of the Prophet data of the summer 1988 campaign are between -20 dB and +20 dB error.

Finally, in Figure 19 the cumulative distribution of the absolute value of the prediction error,  $e'$ , is depicted for the two campaigns. Note that 90.5% of the winter predictions and 88% of the summer predictions are between -20 dB and +20 dB error.

From the above analysis, it is concluded that the accuracy of Prophet 4.0 predictions is better during winter months than during summer months for the "Noncentric" data analyzed.

#### **5. Macroscopic View of All Data Analyzed**

Figure 20 show the frequency distribution of the predicted error,  $e$ . The standard deviation of the error is 15.23 dB, and the median error -14.5 dB. In Figure 21, the

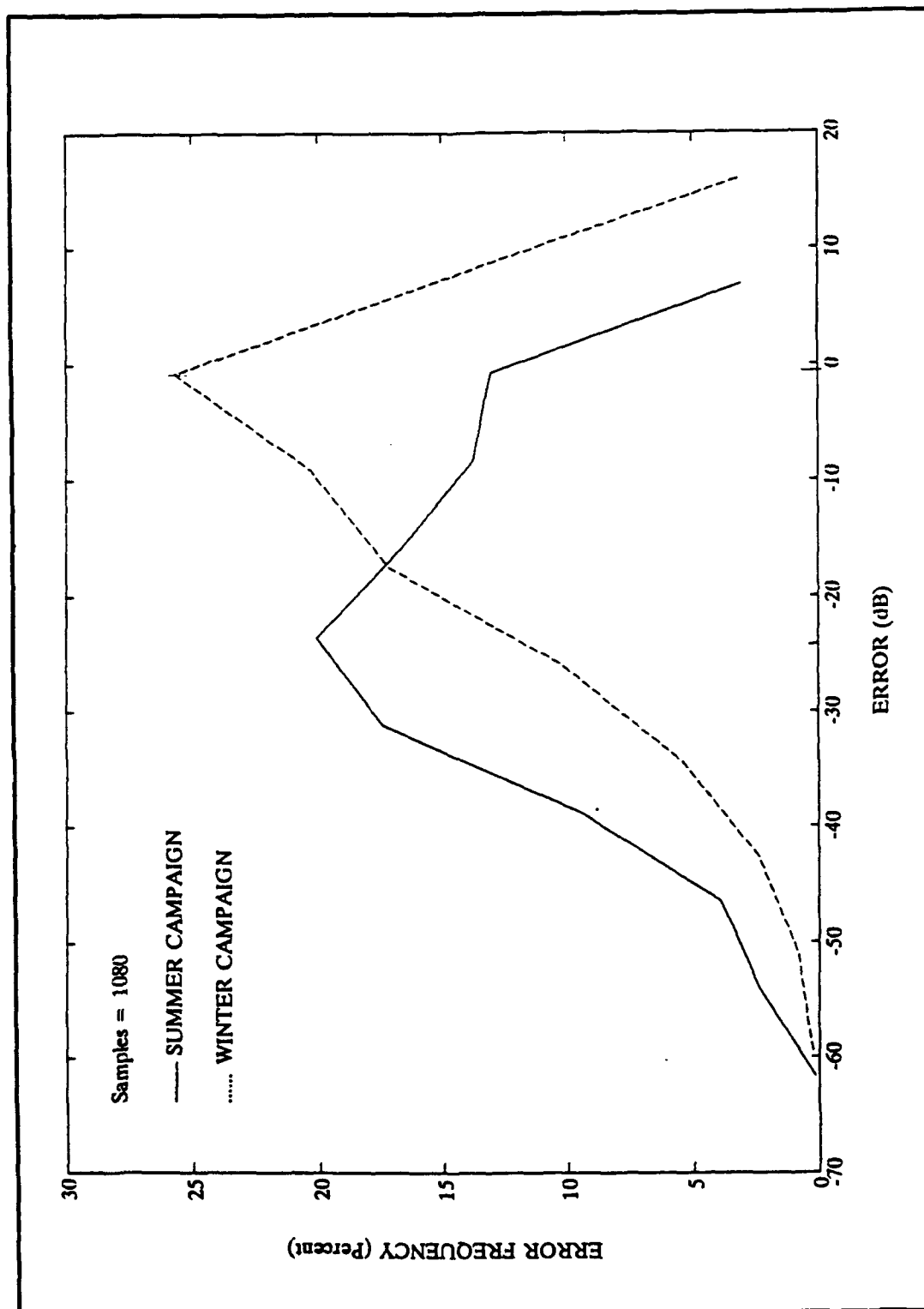
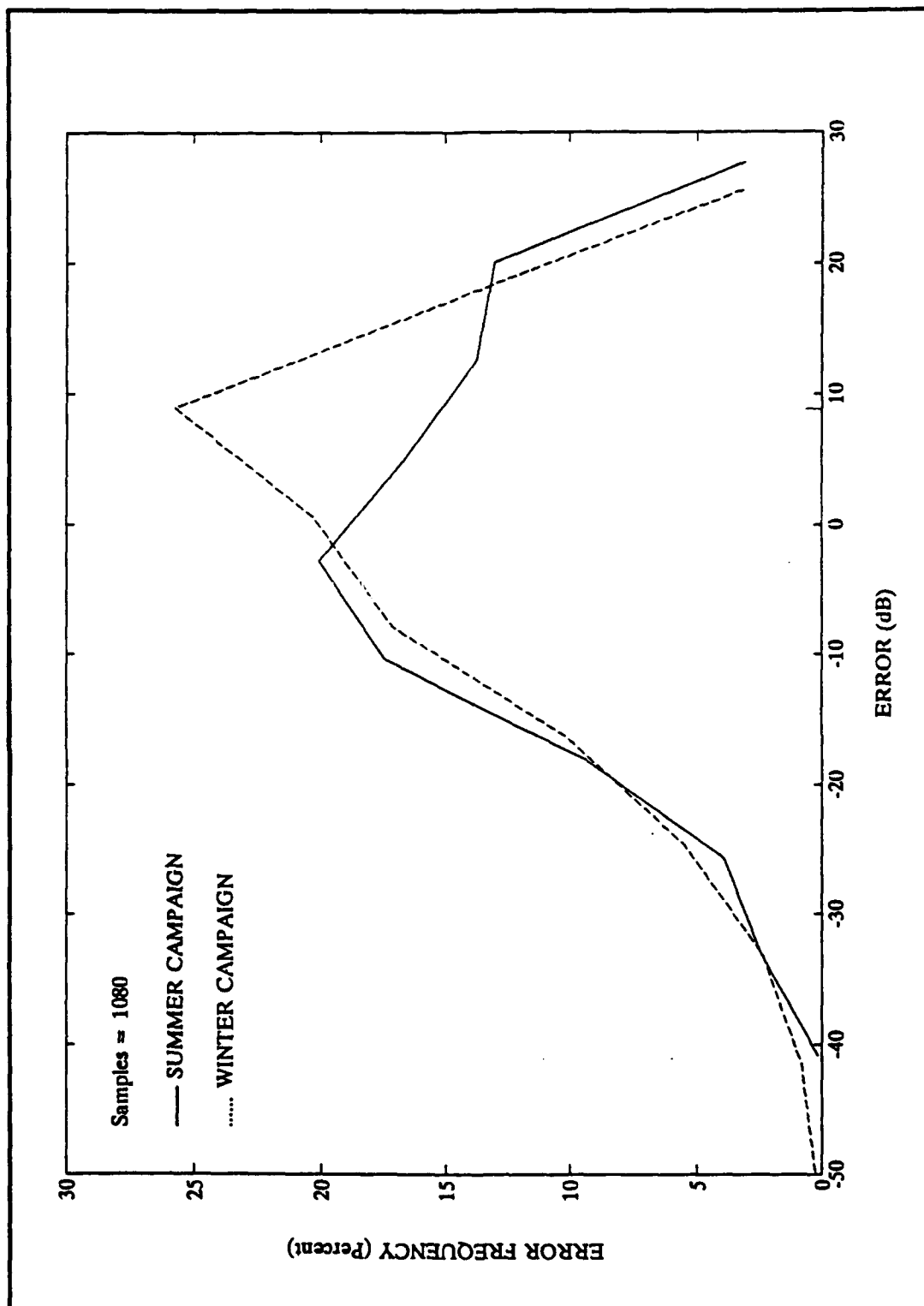


Figure 16. Frequency distribution of the Prophet prediction error,  $e$ , for the two campaigns.



**Figure 17. Frequency distribution of the Prophet prediction error,  $e'$ , for the two campaigns.**

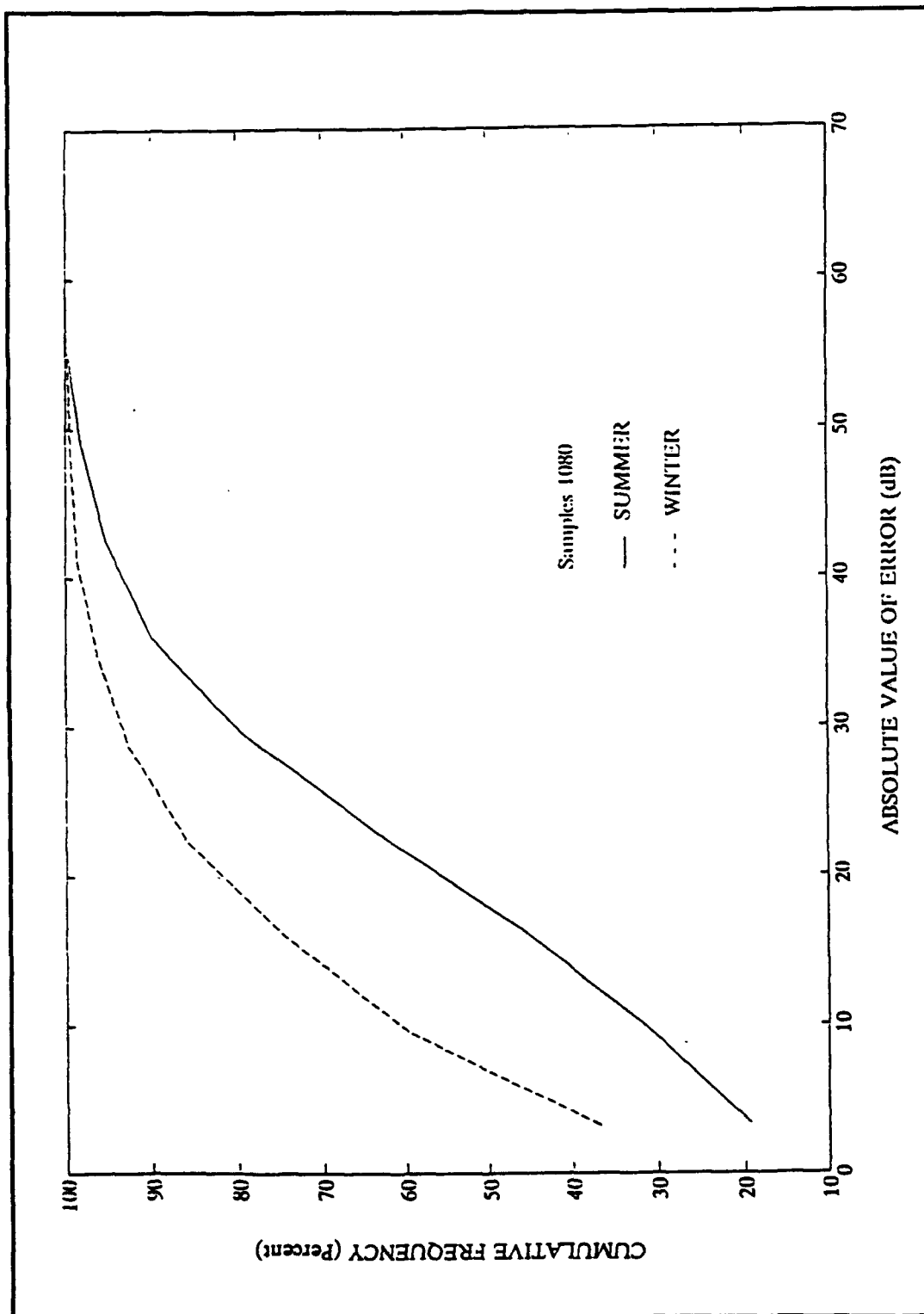


Figure 18. Cumulative distribution of the absolute value of the prediction error,  $e$ , for the two campaigns.

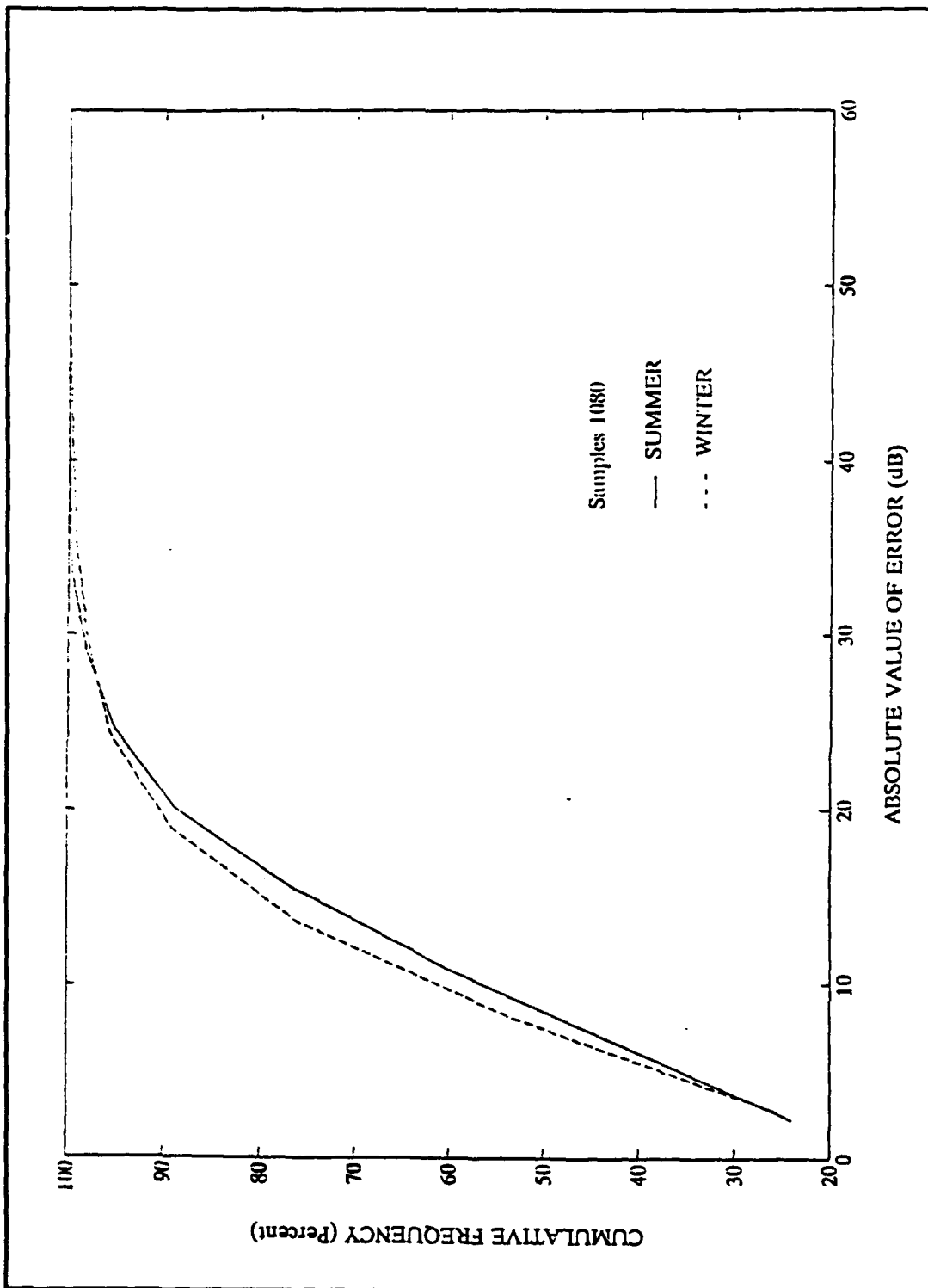


Figure 19. Cumulative distribution of the absolute value of the Prophet prediction error,  $e'$ , for the two campaigns.

frequency distribution of the predicted error,  $e'$ , for all the data analyzed, may be seen. The median error is now 0.77 dB, and the standard deviation of the predicted error is 14.17 dB.

Finally, Figure 22 illustrates the cumulative distribution of the absolute value of the predicted error,  $e$ , (solid curve), and the cumulative distribution of the predicted error,  $e'$ , (dashed curve). It is seen (for the case of  $e$ ) that 70% of the predicted data are between -20 dB and +20 dB error while (for the case of  $e'$ ) 90% of Prophet's predictions are between -20 dB and +20 dB error.

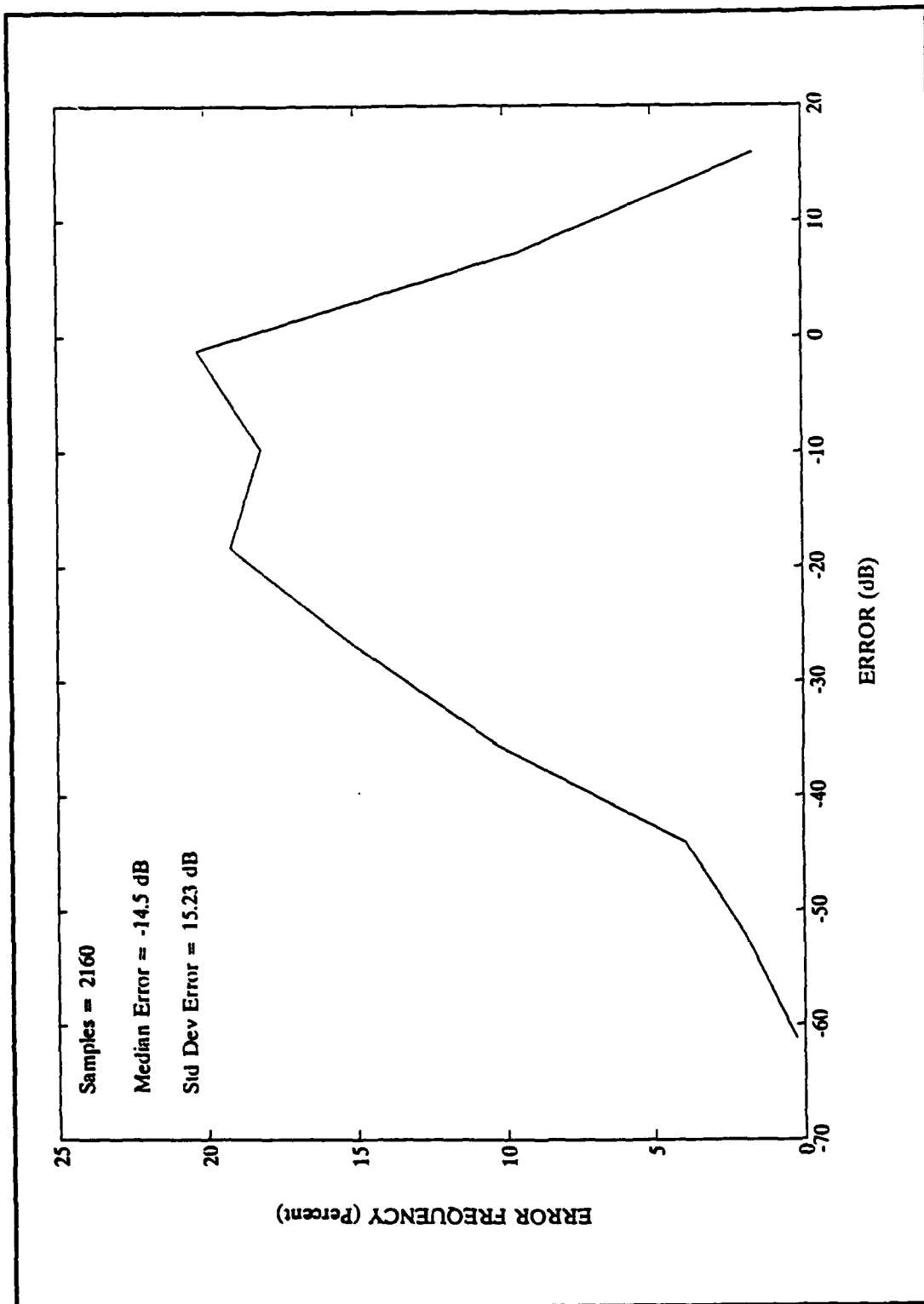


Figure 20. Frequency distribution of the Prophet prediction error,  $e$ , for all the data analyzed.



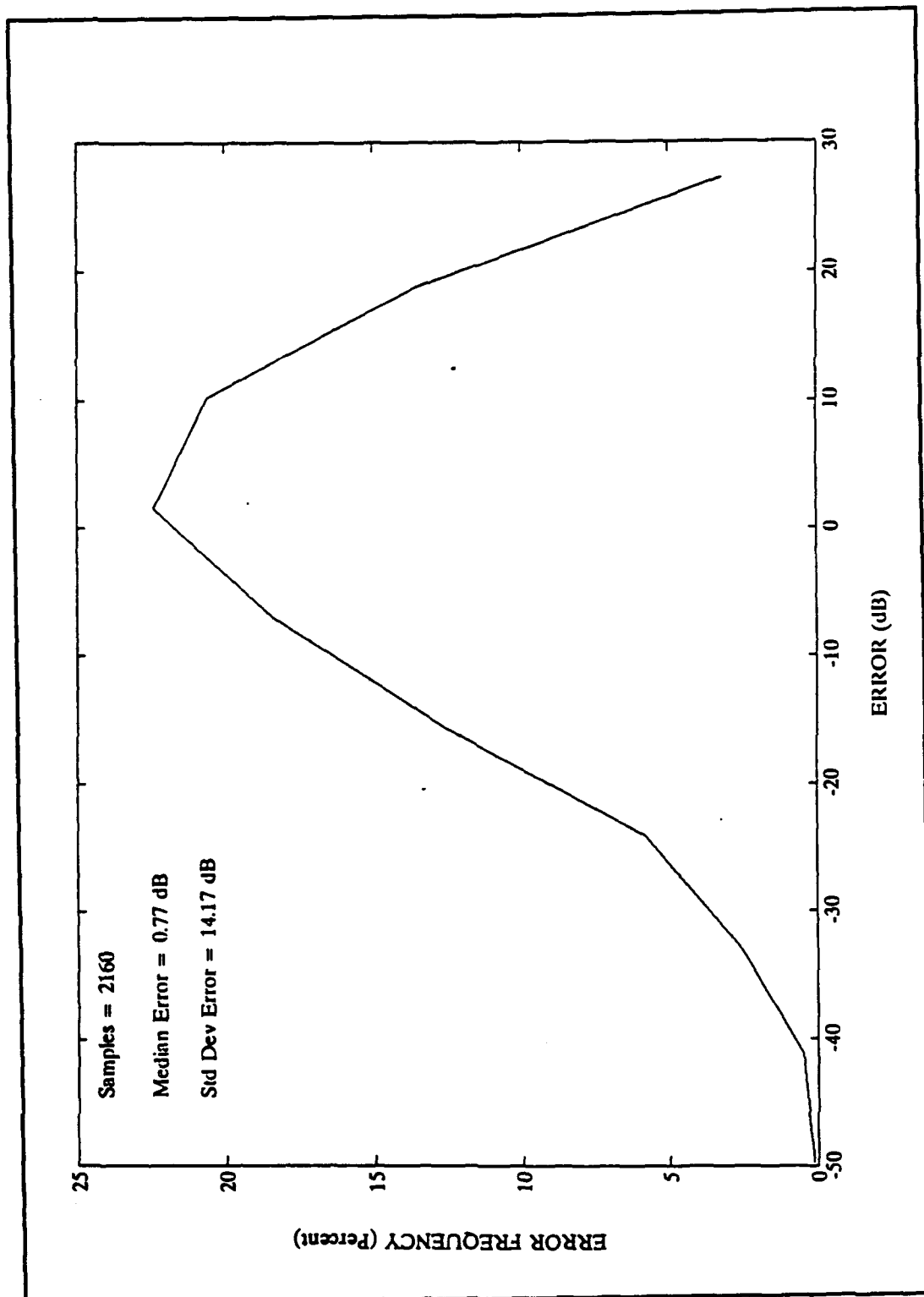


Figure 21. Frequency distribution of the Prophet prediction error,  $e'$ , for all the data analysed.

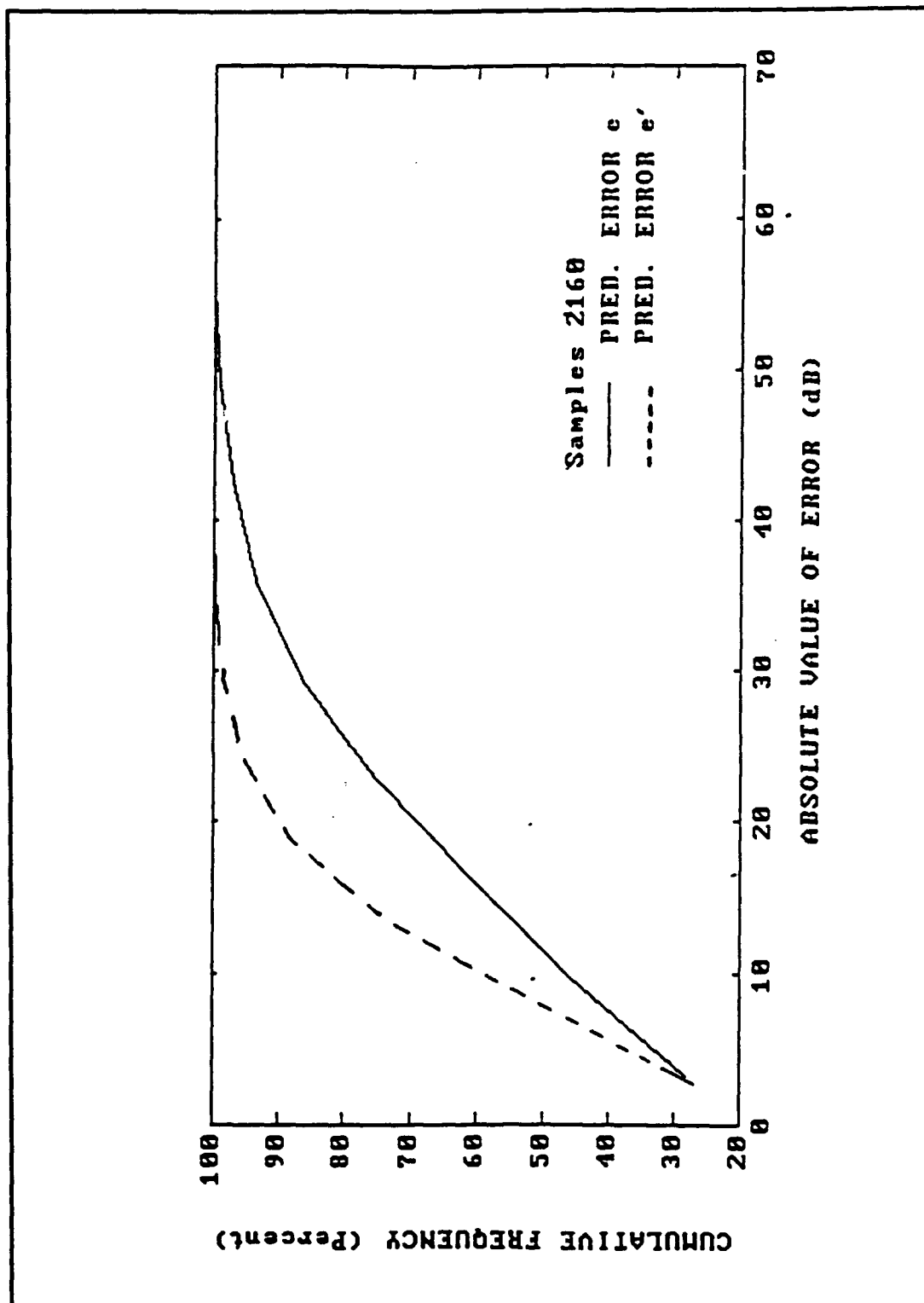


Figure 22. Cumulative distribution of the absolute value of Prophet prediction errors,  $e$ , and  $e'$ .

## V. CONCLUSIONS AND RECOMMENDATIONS

The sloping-vee receiving antenna was simulated and analyzed using the Numerical Electromagnetics Code (NEC). The radiation patterns and input impedance were as expected from the theory of traveling-wave antennas.

Advanced Prophet 4.0 predictions are, in general, more accurate in winter than in summer for polar paths.

Considering the variability of the polar ionosphere, the accuracy of Advanced Prophet's predictions for the simulated Clyde River-Leicester shortwave link is reasonable.

Further evaluation of propagation prediction programs for polar paths should be conducted. Some of the programs are:

The propagation model AMBCOM is available at NPS. It has an algorithm for computing the electron density profile in the high-latitude ionosphere and a model for auroral absorption, and is currently under evaluation.

A new version of IONCAP-PC for polar regions, ICEPAC, is also available and will be evaluated during 1991.

The "Noncentric" database provides a long-needed source of polar data for the evaluation of the above prediction models. However, the "Noncentric" data are not measurements of the incoming field strength but of signal-to-noise at the receiver input terminals. This is a major "shortcoming" of the database

which will affect the quality of the evaluation of prediction models.

It is recommended that any future data collected must accurately relate received field strength to receiver input voltage.

A database involving several types of polar paths would be better for the evaluation process. The areas of interest for the location of transmitter and the receiver are: the polar cap, the auroral oval, the auroral trough, or outside of the above three. Thus, a total of 16 different paths are possible and should be considered carefully in planning future evaluation of high-latitude prediction codes.

## **APPENDIX A   ELEMENTS OF SHORTWAVE THEORY**

### **A.   GROUND WAVE PROPAGATION**

The lower part of the HF band (2-5 MHz) can be used for communications by means of ground wave. Ground wave theory ignores the effects of the ionosphere and assumes that the propagation path is around a spherical earth with homogeneous parameters. Ground wave is affected primarily by the electrical characteristics of the ground (conductivity and dielectric constant), climate, vegetation and the polarization of the wave (vertically polarized fields are most suitable for ground wave propagation). A characteristic feature of ground wave is that it is independent of diurnal and seasonal variations. The ranges obtained by ground wave propagation are determined by the attenuation of fields and are strongly dependent on the operating frequency. (Lower frequencies propagate over greater distances).

### **B.   SKYWAVE PROPAGATION**

Skywave propagation is more important than ground wave since it supports very long distance paths which often reach several thousand kilometers. The transmitted wave utilizes certain properties of the ionosphere as it is reflected back to earth.

## 1. Structure of the Ionosphere

The ionosphere, located up in the stratosphere, blankets the earth and consists of several electrically conducting layers that vary widely over the earth's surface. The formation and intensity of these ionized layers are primarily due to electromagnetic radiation from the sun extending over the ultra-violet and X-ray portions of the spectrum. Here sufficient quantities of electrons and positive ions reflect the radio waves. The ability of the various layers to reflect HF waves becomes stronger as the radiation from the sun increases; at the same time, though, the attenuation of the transmitted wave also increases.

The solar radiation varies considerably with the geographic latitude, the time of day, the season and the sunspot activity. The immediate effect of this variability is a change in the possibility of propagation being supported for certain frequencies. The ionosphere is divided into three regions, or layers, designated as D, E and F layers.

### a. The D-layer

The D-region is located at an altitude of 60 to 90 km. It has a comparatively low free- electron density of about  $10^9$  e/m<sup>3</sup>, compared with a much higher molecular density of about  $10^{20}$  mol/m<sup>3</sup>. The D-layer is a day-time phenomenon. It appears after sunrise and attains its strongest ionization shortly after local noon. During afternoon and evening hours

the layer gradually breaks down and is neutralized after sunset. There is also a seasonal variation in the D-layer electron densities with maximum value in summer.

D-layer ionization is not sufficient to reflect shortwaves therefore penetration occurs. The relatively high electron collision frequency in this region is the main cause for the absorption on the D-layer. This attenuation of shortwaves in the D-region during daytime hours determines achievable ranges and transmitter powers necessary for a transmission.

#### b. The E-layer

The E-layer spans the altitude range from 90 to 130 Km above the earth. Maximum ionization takes place at 110 Km. The E-layer has a pronounced diurnal variation with maximum electron density around noon. At night, only a small residual level of ionization remains and it has virtually ceased to have any effect in shortwave propagation. The distances attained via the E-layer for daytime propagation are less than 2000 Km.

In addition to the regular E-layer, there is also the sporadic-E layer,  $E_s$ , named after its transient and irregular nature. It is situated 120 Km above the earth and exhibits very high ion concentration. Its occurrence depends largely on the geographical latitude. Thus, it is essentially a daytime phenomenon in low latitudes with no significant

seasonal variation. Conversely, in high latitudes it occurs only at nighttime. In middle latitudes the formation of  $E_s$  is more frequent by day than by night and more in summer than in winter. Because of these variations, the study of sporadic-E is done by statistical means. The high ionization of  $E_s$  enables frequencies well above 30 MHz to be transmitted (VHF band).

### c. The F-layer

The F-layer is very important for shortwave communications because of the large attainable distances. It is divided into the F1 and F2 sublayers.

The F1-layer occupies the altitude region from 150 to 220 Km above the earth and exists only during the day. It is more pronounced in summer than in winter, and at high sunspot numbers. The F1-layer occasionally reflects shortwaves, but, usually, they penetrate the F1 region and are reflected by the F2-layer.

The F2-layer is located 225 to 450 Km above the earth and is the principal reflecting region for long distance shortwave communications. In contrast to the E and F1-layers, the F2-layer does not disappear after sunset and a residual ionization remains. Thus, during the night, HF propagation is only possible because of the F2-layer. The height and ionization of the F2-layer vary diurnally and seasonally with maximum height in summer and minimum in winter. Figure 2 shows



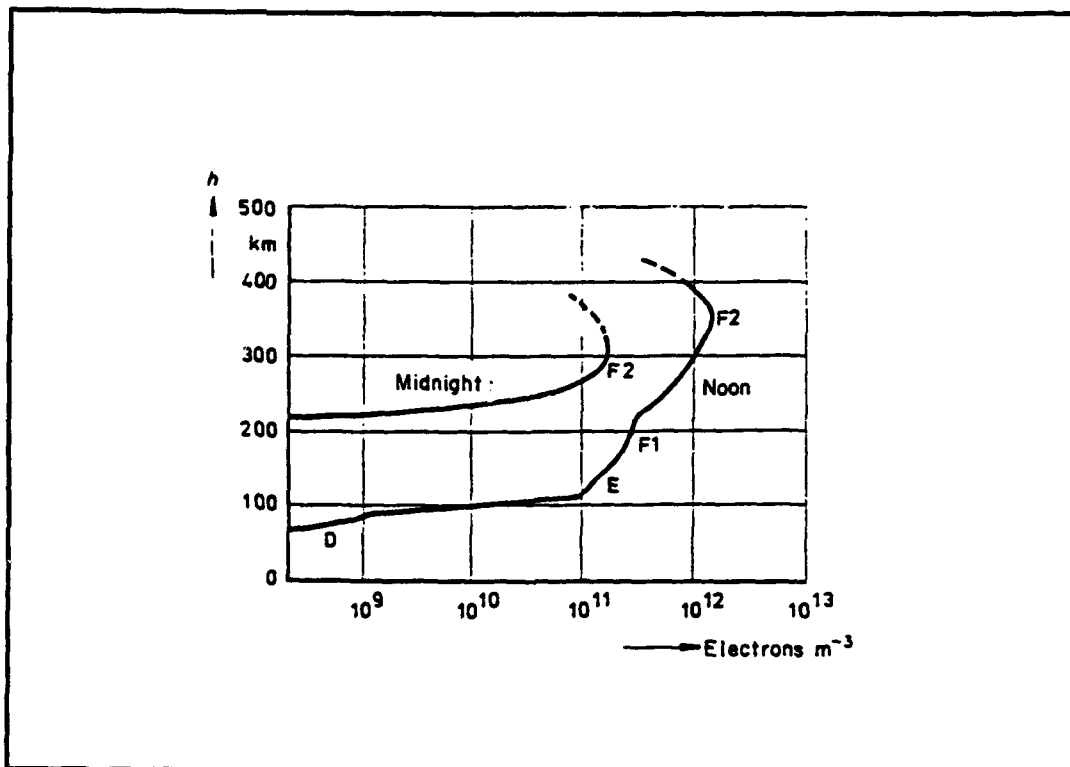


**Figure 23.** Diurnal variation of electron density and the formation of ionospheric layers. From [Ref. 12: p. 21].

a typical distribution of the electron density at noon and midnight hours for an undisturbed ionosphere.

## **2. The Propagation of HF-Waves in the Ionosphere**

### **a. Ordinary and Extraordinary waves**

The earth's magnetic field deflects the free electrons in the upper atmosphere from their linear path in such a way as to cause them to move in the form of a spiral around the magnetic lines of force.

The strength of the magnetic field  $B$  ( $\text{Wb/m}^2$ ), as well as the mass  $m$  (gr), and the charge of the electron  $e$

(Cb), are the quantities that determine the angular velocity  $\Omega_H$ , of the electron's spiral movement,

$$\Omega_H = (e/m)B \quad (1)$$

From (1) the frequency is easily obtained ( $\Omega_H = 6.282f_H$ ) and is called gyrofrequency  $f_H$ . In the ionosphere  $f_H = 2.84 \times 10^{10} B$  and varies from 1.7 MHz at the magnetic poles to 0.7 MHz at the magnetic equator [10].

When an electromagnetic wave of frequency  $f$  enters the ionosphere, it is split into two components: the ordinary  $f_o$ , and the extraordinary  $f_x$  wave. These are given respectively by

$$f_o = [f(f + f_H)]^{1/2} , \quad (2)$$

and

$$f_x = [f(f - f_H)]^{1/2} . \quad (3)$$

The polarization of the ordinary and extraordinary waves is circular, moving in opposite directions. The variability of the ionosphere affects the two waves. Their reflections take place at different altitudes; hence, the refractive indices, the delay times and the attenuation are different for the two waves. The extraordinary wave is attenuated more than the ordinary wave.

The two reflected waves, after leaving the ionosphere, recombine to form the originally transmitted wave of frequency  $f$ . Due to the differing attenuation and delay times of the two waves, the polarization of the emitted wave now becomes elliptical.

#### b. Critical Frequency, MUF, FOT, and LUF

Snell's law of refraction shows, that, if a skywave is incident upon the ionosphere at angle  $i_0$  with respect to the normal, the height at which the reflection occurs has a refractive index,  $n_x$ , equal to  $\sin(i_0)$ . For vertical incidence  $i_0 = 0$ , which means that  $\sin(i_0) = 0$ , and thus the reflection will occur at the height where  $n_x = 0$ . It is known [10], that  $n_x$  is given by

$$n_x = [1 - (81N_x / f^2)]^{1/2} , \quad (4)$$

where  $N_x$  is the number of free electrons per cubic meter available for conduction, and  $f$  is the operating frequency in MHz.

For the vertical case  $n_x = 0$ , and (4) can be utilized to obtain the highest frequency that is reflected by the ionosphere at a location when  $N_x$  is maximum,

$$f_c = 9(N_{\max})^{1/2} . \quad (5)$$

This frequency is called the critical frequency or plasma frequency. The critical frequencies of the E, F1 and F2

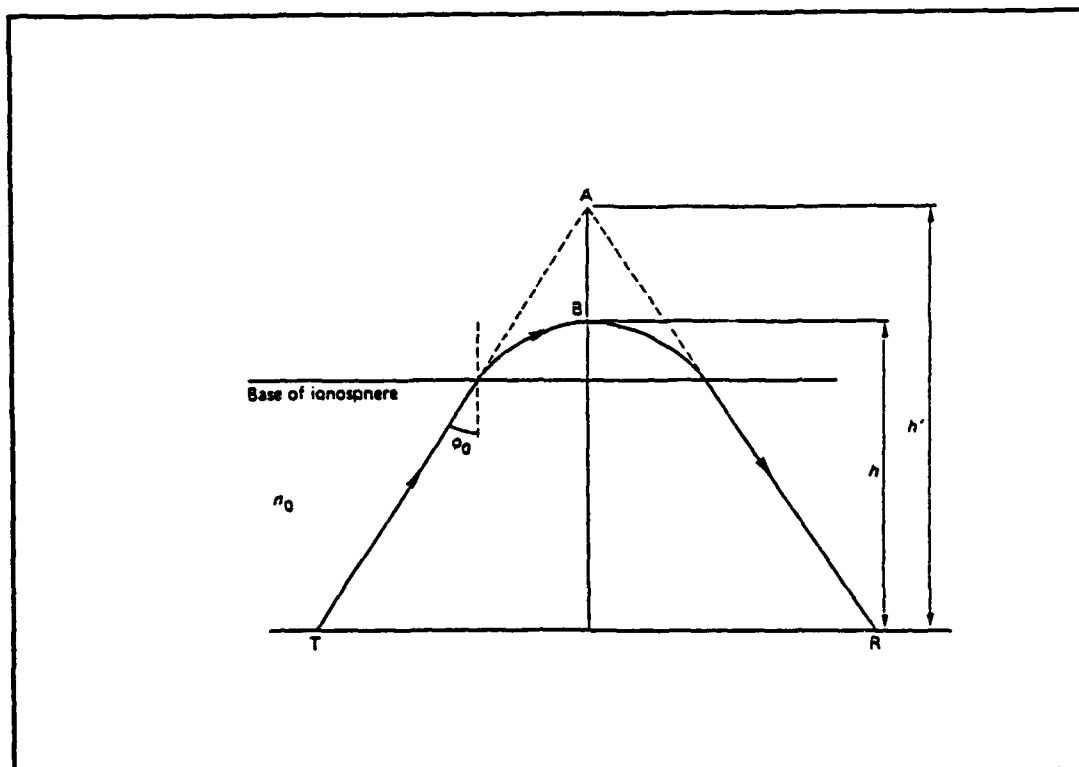
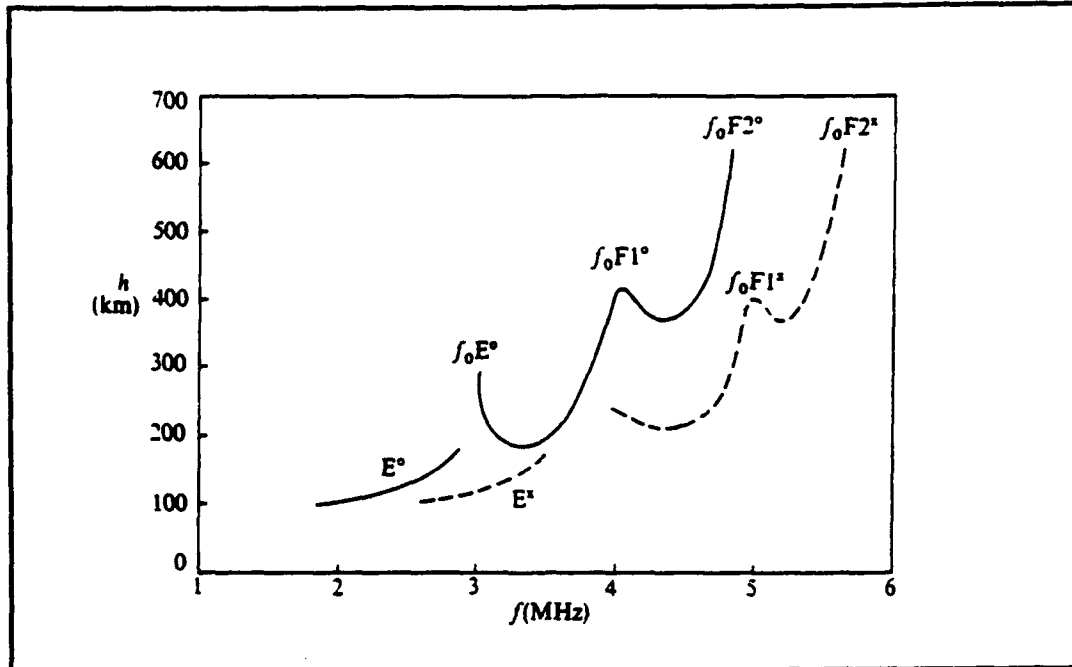


Figure 24. The true reflection height  $h$ , and the virtual height  $h'$ . From [Ref. 11: p. 63].

layers are written respectively as  $f_oE$ ,  $f_oF1$  and  $f_oF2$ .

Many important characteristics of the ionosphere are determined from the critical frequencies and the virtual heights of the layers. An electronic device called ionosonde measures the virtual height  $h'$  of the ionosphere by using a pulsed-radar technique. This is the height from which the wave would appear to be reflected if the ionosphere were a perfect reflector. Figure 24 illustrates a ray path through the ionosphere and the virtual height  $h'$ . If a number of measurements are made by the ionosonde, the reflection height  $h$  against frequency  $f$  can be plotted. This is called an ionogram. In Figure 25 an ionogram can be seen which indicates



**Figure 25. A typical ionogram. The superscripts o and x refer to ordinary and extraordinary waves. From [Ref.10: p. 79].**

reflection from E, F1 and F2 layers for both ordinary and extraordinary waves.

If the angle of incidence,  $i_o$ , of the electromagnetic wave is not zero, the refractive index,  $n_x$ , at the height at which reflection occurs, is given by

$$n_x = \sin(i_o) = [1 - (f_c / \text{MUF})^2]^{1/2} , \quad (6)$$

where MUF is called the maximum usable frequency and is the highest frequency to be reflected from the ionosphere. Frequencies higher than MUF are not reflected, but, instead, penetrate the various layers and propagate into space. The MUF depends on the specific path, the angle of incidence of the shortwave with the ionosphere, the time of day, the season,

and the solar activity. The MUF, at any distance, is determined by multiplying the critical frequency at zero distance by a MUF factor which related to the secant of the angle of incidence. Figure 26 shows the MUF factor vs range for the various ionospheric layers. The distance that can be spanned by the MUF is called the skip distance.

To account for the MUF variations, the frequency of optimum transmission (FOT) is usually used. The FOT is chosen to be 85% of the MUF.

Another quantity is the lowest usable frequency, (LUF), which depends on the engineering characteristics of the shortwave link. LUF is the frequency limit below which the signal-to-noise ratio does not have an acceptable value.

#### c. Variation of the Critical Frequencies

(1) Solar activity dependence. Sunspots have a major effect on the ionization level of the ionospheric layers. If the sunspot number is high, the radiation of the sun is also high as is the intensity of ionization of D, E, and F layers. This means that the attenuation of HF waves in the D region increases with the sunspot number, and that higher frequencies can be reflected by the E and F regions.

To measure the sunspot number, the relative Zurich sunspot number (ZSN), R, is used. It is given by

$$R = k(10g + s) , \quad (7)$$

where

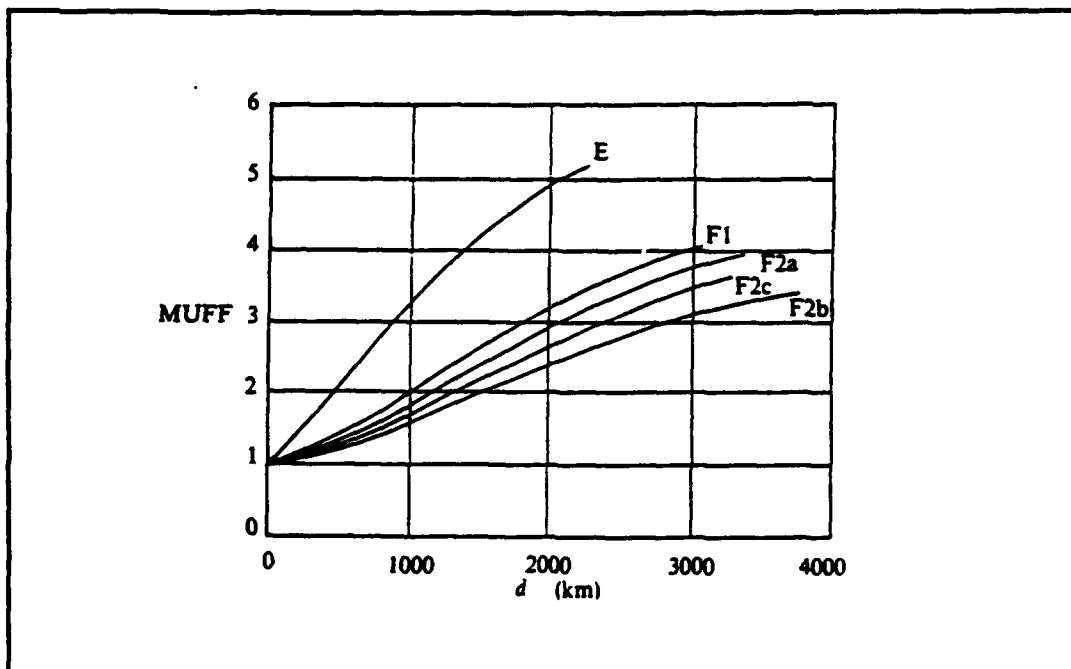


**Figure 26. The MUF factor MUFF, versus range d. The layers F2a and F2b represent winter day and night respectively, and F2c a summer day or night. From [Ref. 10: p. 82].**

$g$  is the number of sunspot groups,

$s$  is the number of single spots, and

$k$  is the equipment's correction factor.

The sunspot number fluctuates sharply from day to day; thus, for the planning of shortwave links, the twelve-month average value  $R_{12}$ , is used. Figure 6 shows the dependence of the critical frequencies on the average sunspot number  $R_{12}$ .

Measurements since 1749 show that sunspot maxima and minima follow an 11-year cycle on the average. There is a pronounced correlation of the F2-layer critical frequency with the eleven year solar cycle. This can be seen in Figure 7 for the monthly mean noon critical frequencies as observed at Slough [Ref. 11], over the last solar cycle

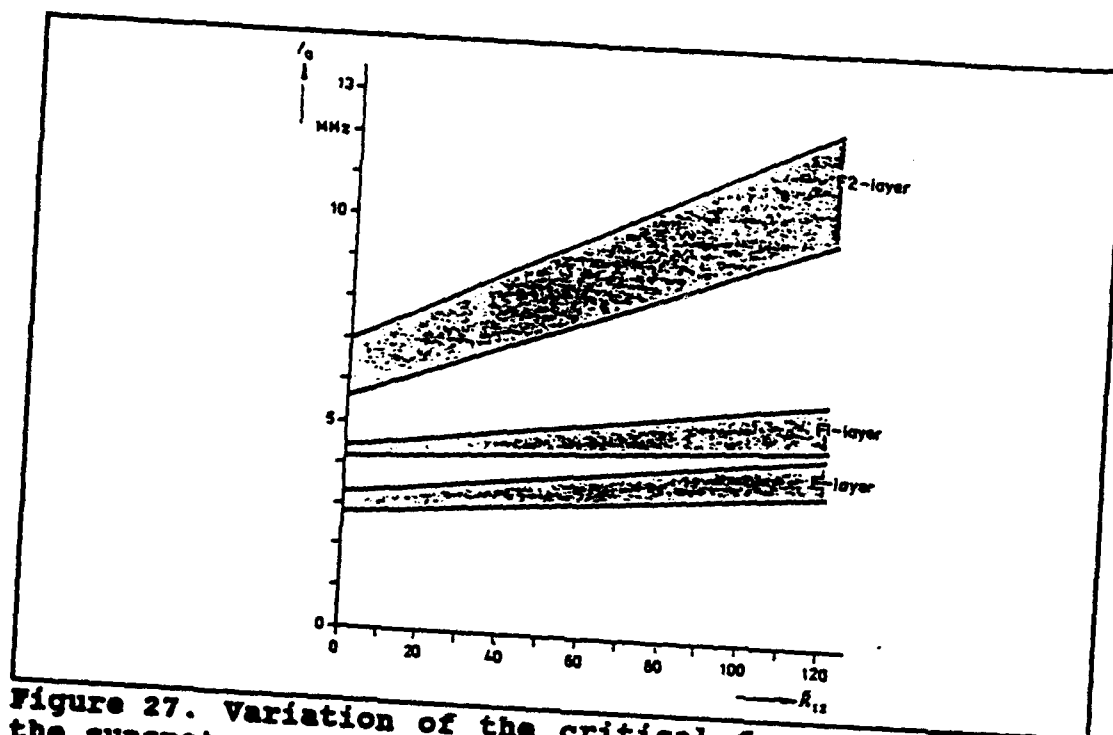


Figure 27. Variation of the critical frequency  $f_o$ , with the sunspot number. From [Ref. 12: p. 23].

(1970-1981).

(2) Time variations. The critical frequencies vary annually, seasonally and diurnally. Critical frequencies during years of low sunspot activity are limited to values at the lower part of the HF band. On the other hand, the critical frequencies of the years of high sunspot activity have much higher values.

The seasonal variations of  $f_oE$  and  $f_oF1$  are in phase with solar zenith angle  $\chi$ . This means that they are greater in the summer months. The opposite takes place for the  $f_oF2$  which is in antiphase [13]. This is known as the winter anomaly and occurs in daytime only.



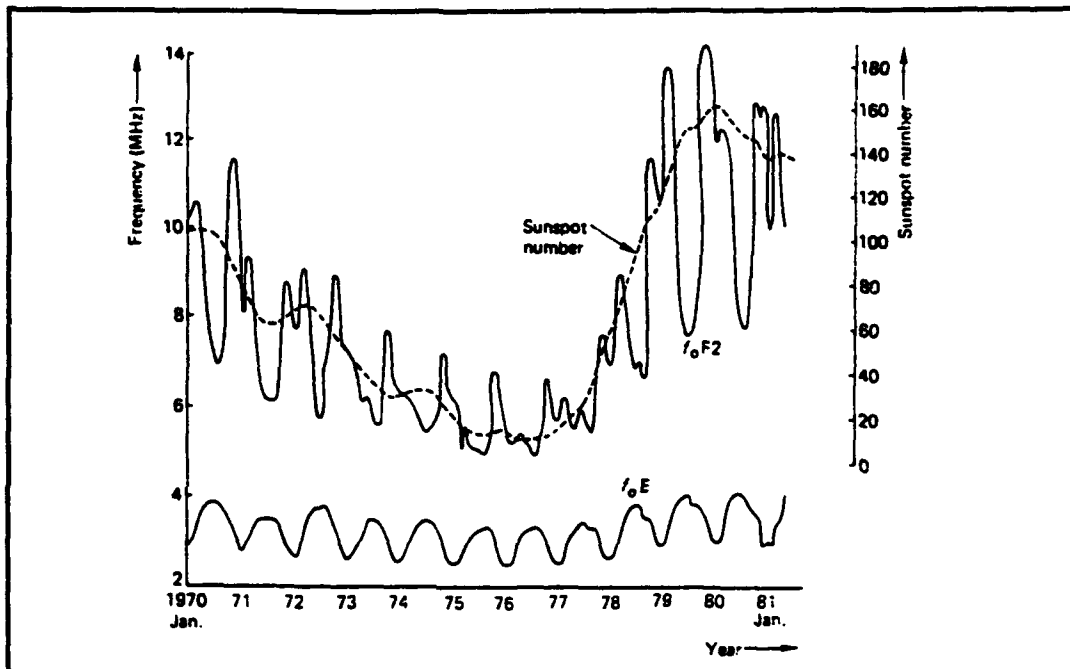


**Figure 28. Monthly mean of the noon critical frequencies observed at Slough during the last sunspot cycle 1970-1981. From [Ref. 11: p. 68].**

Figure 29 shows diurnal variation of monthly median  $f_oF2$  for four months and three years of high, medium, and low sunspot activity as measured at Slough [11]. Diurnal variations are usually observed during winter months.

#### d. Propagation modes of the Skywave

The radiation patterns of the transmitting antenna and the operating frequency of the shortwave link determine which one of the several possible paths the HF ray will follow. Figure 30 shows six different ray paths as a function of elevation angle for a fixed frequency. The range decreases as the elevation angle increases (case 1 to 3) until the skip distance is reached. If, however, the elevation angle is

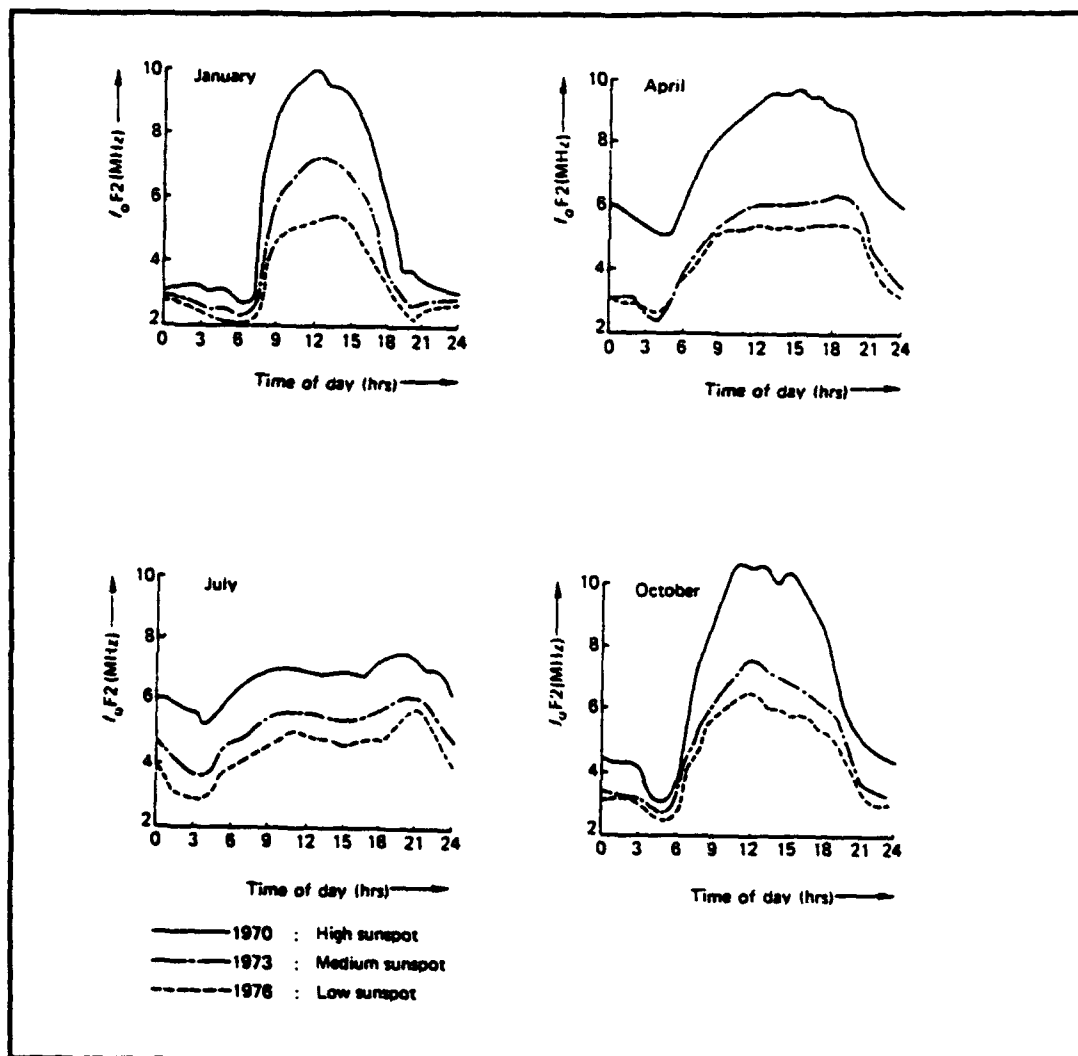
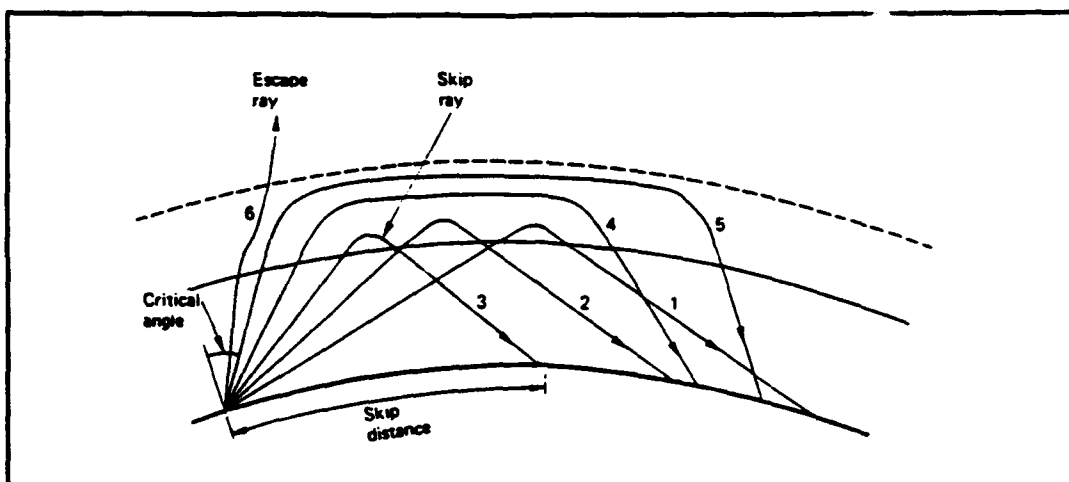


Figure 29. Diurnal variation of monthly median  $f_oF2$  observed at Slough. From [Ref. 11: p. 73].

further increased, the rays would be trapped in the ionosphere, and the attainable ranges would increase rapidly (case 4, 5). For still higher angles, a critical angle of incidence is reached beyond which penetration of the layer occurs (case 6).

When the shortwave link has several hundred Km length, several hops are necessary. The electron



**Figure 30. Ray paths against launch angles for a fixed frequency. From [Ref. 11: p. 62].**

concentration, and thus the ionization of the ionospheric layers, is different for the individual sections of the path. This means that different transmission conditions take place along the path. In Figure 31, examples of possible radiation paths for multi-hop links can be seen.

In multi-path propagation, several signals arrive at the receiver with different time spacings. This time dispersion is an inherent characteristic of multi-path propagation. The causes of time dispersion include the following:

- (a) Ground wave/skywave interference (short links).
- (b) Skywave reflections from E and F layers.
- (c) Multi-hop links (see Figure 9).
- (d) Different elevation angle skywave paths.
- (e) Splitting of the skywave into the ordinary and extraordinary wave.

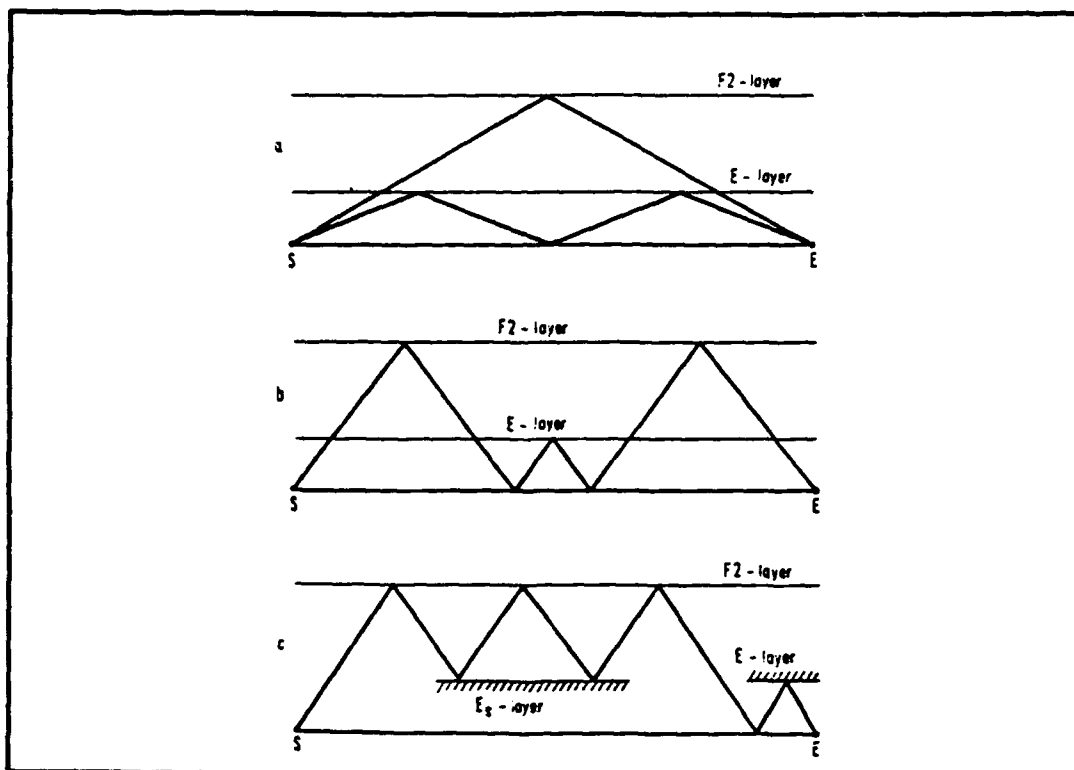


**Figure 31. Various propagation modes for multi-hop links.**  
From [Ref. 12: p. 41].

Time dispersion is associated with a degraded channel performance in terms of error rate. High error rates occur as a result of intersymbol interference.

### 3. Losses and Field Strengths in a Shortwave System

The received signal power,  $S$  in dBW at the output of the receiving antenna of a shortwave link is given by

$$S_{dB} = P_t + n_t + D_t - L_{\text{sys}} + n_r + D_r, \quad (8)$$

where

$P_t$  = transmitter power (dBW),

$L_{\text{sys}}$  = path loss in the given direction (dB),

$n_t$  = transmitting antenna efficiency (dB),

$\eta_r$  = receiving antenna efficiency (dB),

$D_t$  = transmitting antenna directivity (dB), and

$D_r$  = receiving antenna directivity (dB).

Assuming that a shortwave system begins with the transmitter output and terminates with the receiver input (i.e. a closed transmission system), its total loss  $L_{\text{sys}}$  in dB follows the formula [12],

$$L_{\text{sys}} = L_{\text{fr}} + L_1 + L_g + Y_f - (G_t - G_r) , \quad (9)$$

where

$L_{\text{fr}}$  = losses due to attenuation in free space between the transmitting and receiving antennas (dB),

$L_1$  = losses in the ionosphere (dB),

$L_g$  = losses due to the reflection on the ground (dB),

$Y_f$  = fading reserves (dB),

$G_t$  = gain of the transmitting antenna (dBi), and

$G_r$  = gain of the receiving antenna (dBi).

Referred to isotropic transmitting and receiving antennas, the free space attenuation is given by

$$L_{\text{fr}} = 20 \log(4\pi d_{\text{km}} c / f) , \quad (10)$$

where

$d_{\text{km}}$  = path length in Km,

$f$  = operating frequency in MHz, and

$c$  = speed of light ( $3 \times 10^8$  m/sec).

As mentioned above, the emitted electromagnetic wave on its way to E or F reflecting layers, passes through the D-layer where it suffers substantial losses due to absorption. These losses depend on the sunspot number  $R$ , and the zenith angle of the sun  $\chi$ . To calculate the ionospheric losses, the absorption index  $I$  is used [12],

$$I = (1 + 0.0037R) \cdot [\cos(0.881\chi)]^{1.3} . \quad (11)$$

The absorption index is higher in winter than in summer due to the winter anomaly. With the aid of a nomogram found in [12] and entering with the absorption index  $I$  and the elevation angle of radiation, the ionospheric losses  $L_f$  can be determined.

The reflection of a skywave by the ionosphere changes its polarization considerably. Thus, the reflected wave reaches the ground with different polarization than the emitted one. Assuming that the two components of the energy of the incident wave are equal, then the losses due to reflection on the ground are given [12] by

$$L_g = 10 \log[(R_v^2 + R_h^2) / 2] , \quad (12)$$

where  $R_v^2$  and  $R_h^2$  are the reflection coefficients of the vertical and horizontal component respectively.

The fading of the skywaves is related to changes in the ionosphere. Various kinds of fading are defined according

to their origin; for example, absorption fading, polarization fading, etc. Due to fading, the field strength at the receiving point is continuously fluctuating. It is found [11], that the amplitudes of field strength values undergoing short-period changes follow a Rayleigh distribution. To take into account the field strength variations, a fading reserve  $\gamma_f$  of 14 dB is generally recommended by CCIR for HF links (see eq. 9).

Continuing the analysis of a shortwave system, the received noise in dBW in the receiver bandwidth B is

$$N = kT + B + F_a + n_r + D_n , \quad (13)$$

where

$kT$  = thermal noise power density (-204 dB/Hz),

$B$  = receiver bandwidth (dBHz),

$F_a$  = effective antenna noise power factor (dB), and

$D_n$  = receiving antenna directivity factor for the noise sources (dB).

Thus, combining equations (8) and (13), the received signal-to-noise ratio in the bandwidth B can be found as

$$(S/N)_{dB} = S - N = E_p - L_{\text{sys}} + D_r - N_i , \quad (14)$$

where

$E_p = P_t + n_t + D_t$  , is the effective radiated power,

$D_r = D_r - D_n$  , is the receiving antenna directivity factor against noise, and

$N_i = kT + B + F_a$  is the noise power at the antenna input.

In accordance with the expected grade of service, it is necessary to adopt a minimum required signal-to-noise ratio. Signals that manage to reach or exceed this threshold value are considered successful transmissions.

#### C. POLAR AND AURORAL REGION EFFECTS ON HF PROPAGATION

The high latitude ionosphere is very unpredictable, irregular, and variable in nature. These variations and irregularities have an important influence on HF waves that traverse the auroral and polar regions. In some occasions, the HF signals may be attenuated as much as 200 dB, and the effect in communications is catastrophic.

By way of introduction the terms that frequently occur in the technical literature will be briefly explained.

(a) Solar flare: A burst of light occurring in the chromosphere of the sun and in proximity to a sunspot. Solar flares are accompanied by strong X-ray emission. Flares frequently occur at the peak of the sunspot cycle.

(b) Visual aurora: The luminosity that can be seen in high latitudes (the optical result of the interaction of incoming particles with the atmospheric constituents).

(c) Auroral oval: The region of latitudes containing the visual aurora at a specific time.

(d) Polar cap: The region inside the auroral oval.



(e) Auroral zones: The regions of the earth where the visible aurora occurs most often; in other words, the auroral zone represents the average location of the aurora.

(f) Solar wind: A stream of plasma that originates from the sun. It is composed basically of electrons and protons (95%), and alpha-particles (5%). The solar wind is the principal medium through which the solar activity is transferred to earth; and, as such, is extremely important in solar-terrestrial relations.

(g) Magnetosphere: The pressure of the solar wind which is in motion towards the earth, distorting the terrestrial magnetic field (geomagnetic field), and confining it to a finite region called magnetosphere. In this region, the geomagnetic field exerts a pronounced influence.

(h) Sudden ionospheric disturbances (SID): At times, a solar flare produces abnormally high ionization density in the D-layer. This phenomenon results in a sudden increase in the absorption of shortwaves and fading may occur. These shortwave fadeouts (SWF) may last from a few minutes to a few hours and occur only on the sunlit side of the earth. In general, SIDs depend on the solar zenith angle. SID absorption is the one of three types, the others being auroral absorption (AA) and polar cap absorption (PCA).

(i) Geomagnetic storms: In addition to the intensified ionization produced by a solar flare, electrically charged particles cause a disturbance of the earth's magnetic field

which may last several days. During these disturbances the components of the earth's magnetic field fluctuate over much wider limits than under undisturbed conditions.

There are two types of geomagnetic storms: Those that occur sporadically and those that exhibit a strong 27-day periodicity. The former type occurs during years of high solar activity, but the recurrent type can be found at any phase of the solar cycle. Geomagnetic disturbances are more intense in the vicinity of auroral zones [13].

Geomagnetic activity exhibits a seasonal variation. Figure 11 illustrates the seasonal distribution of very large geomagnetic storms for the period from 1932 to 1984. Geomagnetic storms occur most frequently during equinoxial months and less frequently during solstitial months.

(j) Ionospheric storms: Large geomagnetic storms are accompanied by a number of ionospheric phenomena such as: reduction of the critical frequency of the F2-layer ( $f_oF_2$ ), possible blackout of HF communications and enhancement of the F and sporadic E layers. These events are also called ionospheric storms.

(k) Substorm: A substorm is a localized night-time phenomenon characterized by the "break up" of visual aurora around midnight and accompanied by abrupt changes in radio-wave absorption.

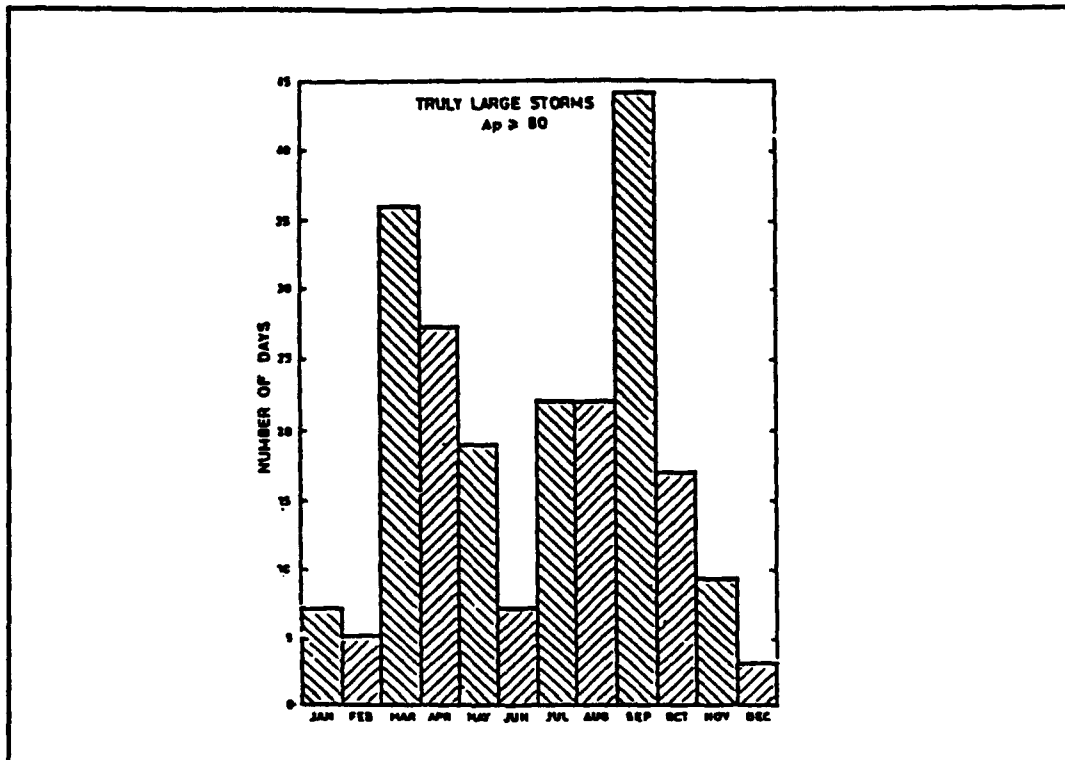


**Figure 32. Seasonal distribution of very large geomagnetic storms from 1932 to 1984. From [Ref. 16: p. 5-32].**

### **1. Auroral Phenomena**

The polar ionosphere is affected mainly by two phenomena: (1) The solar wind induces an electric field in the ionosphere which causes ionization drift; as a consequence a transport of ionization irregularities through the polar cap may occur. (2) Charged corpuscles from the sun and from the upper magnetosphere penetrate the atmosphere and cause enhanced ionization and irregularities at various ionospheric layers.

The principal high-latitude ionospheric irregularities are the following:

### a. Auroral Absorption

This is the form of absorption which occurs most often in polar regions and results from enhanced ionization caused when energetic electrons are precipitated into the upper atmosphere. The reconnection of magnetic field-lines in the magnetosphere is believed to provide such electrons [14] which are forced poleward by the earth's magnetic field during substorms.

Auroral absorption is a sporadic phenomenon that occurs as a series of discrete absorption enhancements lasting from a few minutes to a few hours. It is correlated with geomagnetic and auroral activity (though without exact correspondence). The auroral absorption has a zonal occurrence pattern with a statistical width of  $5^{\circ}$  to  $8^{\circ}$  magnetic latitude and is centered somewhere between  $64^{\circ}$  and  $68^{\circ}$  of magnetic latitude. The precipitated electrons have sufficient energy (more than 20 keV) to reach the E and D regions [15].

The absorption is at maximum level near midnight and in the morning, and at minimum level during the afternoon and early evening. The morning absorption appears about an hour after a substorm and is not correlated with local aurora. On the other hand, midnight absorption is less spread out in time and space than morning, and occurs in short-lived but intense events which are related to the local substorms [16]. Figure 12 gives the probability of a given level of absorption

at 30 MHz being exceeded at a latitude of maximum absorption activity.

A shortwave passing through an ionized layer imparts an oscillatory motion to the electrons which vibrate about a mean position. This oscillation causes an increase in the number of collisions between the electrons and the heavier particles of the ionosphere. As a consequence, energy is transferred into the ionosphere and absorbed from the wave. The rate of absorption is directly related to the number of collisions per oscillation.

The effect of collisions is to make the refractive index  $n$  of the medium complex [17];  $n^2 = (\mu - j\chi)^2$ , where  $\mu$  and  $\chi$  are the real and imaginary parts of  $n$ . For the lower atmosphere  $\mu = 1$ . The total absorption  $A$  (in dB), over a path, is given [17] by

$$A = 4.6 \times 10^{-5} \int \frac{N v dl}{v^2 + (\omega \pm \Omega_H \cos \theta)^2} , \quad (15)$$

where

$N$  = electron density in  $e/m^3$ ,

$\omega$  = angular wave frequency,

$v$  = electron collision frequency,

$\Omega_H$  = gyrofrequency, and

$\theta$  = angle of magnetic field with the direction of propagation.

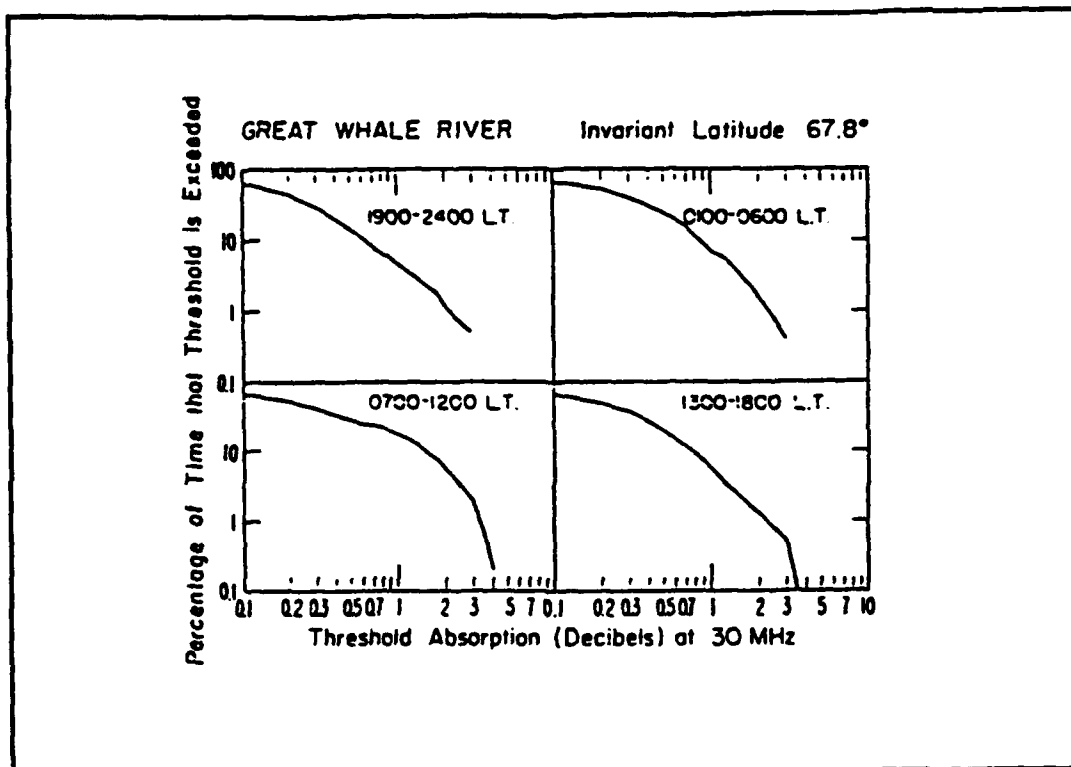


Figure 33. The probability that a given level of absorption will be exceeded at an area of maximum absorption. From [Ref. 17: p. 1357].

The negative and positive sign in the denominator refer to extraordinary and ordinary waves respectively. The absorption is thus greater for the extraordinary wave.

The specific absorption has a maximum at some height which depends on the operating frequency. If the ionization occurs at great height,  $v \ll \omega$  and  $A$  is directly proportional to  $(1/\omega^2)$ . If the height is low,  $v \gg \omega$  and the absorption  $A$  is independent of frequency. In practice, however, the absorption-frequency dependence is expressed as a power law :  $A(f) = Cf^n$ , where  $n$  is determined from

observations with riometers, and C is constant for a given set of data.

#### b. Polar Cap Absorption (PCA)

This type of absorption is due to the abnormal ionization produced from the arrival of energetic charged particles originating at the sun. These charged particles are high-energy solar protons (MeV) emitted during solar flares and are guided poleward by the earth's magnetic field. Polar cap absorption covers the whole region of the polar cap; and, unlike auroral absorption, it is smooth and quite uniform. The duration of PCA varies from 1 to 10 days but usually is 3 days. One of the major characteristics of PCA events is that they are almost always preceded by a major solar flare.

The ionization responsible for PCA lies primarily in the D-layer of the ionosphere. The effect of PCA on HF signals is the very strong attenuation (tens or hundreds dB), resulting in the total black-out of communications. Statistically, however, the HF circuit reliability does not decrease significantly over the 11-year solar cycle. For example, during the 1949-1958 solar cycle, the overall outage due to PCA was 4 to 5% [16]. Figure 34 illustrates the distribution of PCA events for the period 1949 to 1961. The association of PCA with the level of solar activity can be easily seen.

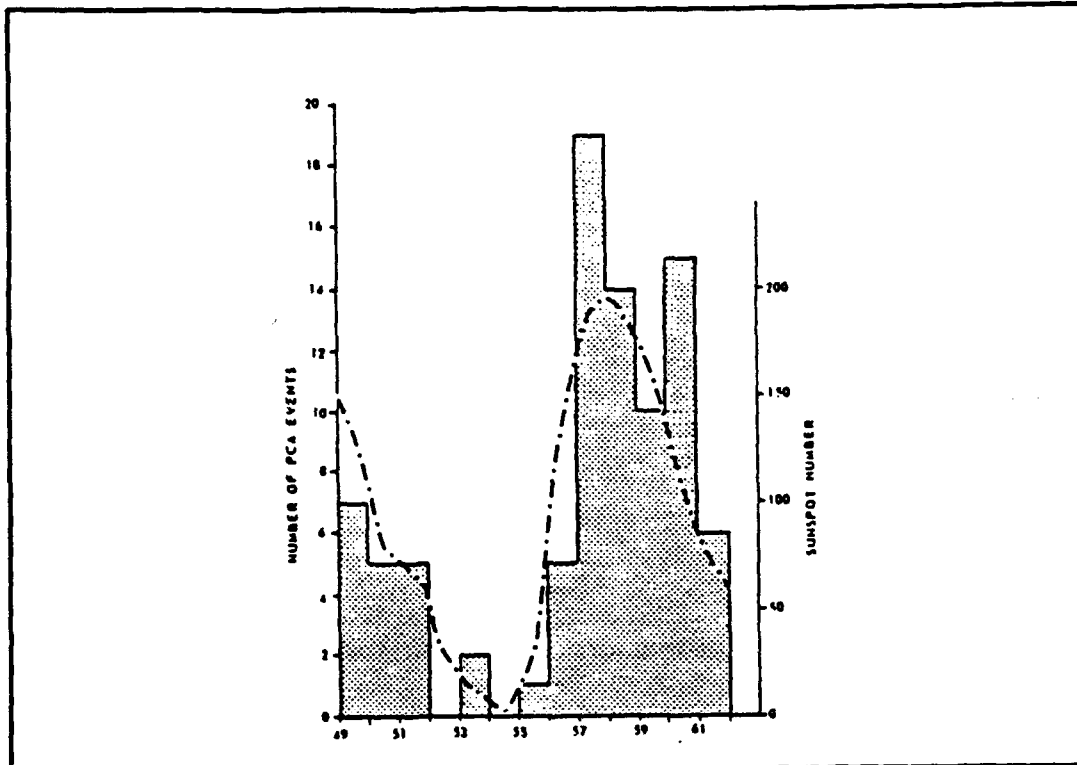


**Figure 34. Association of PCA with the level of solar activity for the period 1949-1961. From [Ref. 13: p. 279].**

A remarkable feature of PCA is the marked diurnal variation in the magnitude of absorption. Thus, reduction in the absorption as much as 4:1 [16] during night hours may occur. This phenomenon is related to the time variation of solar proton intensity due to the conditions in the interplanetary space [18]. The reduction of absorption sometimes makes HF communications possible at night.

PCA events are also called solar protons events (SPE), to emphasize that the solar protons are responsible for the absorption.



### c. F-layer Irregularities

The precipitated soft and hard energetic particles in the polar cap and auroral oval regions, are responsible for the F-layer irregularities. There are large and small scale irregularities. The large form of irregularity, called a "blob", has a horizontal shape and consists of discrete patches of enhanced ionization. The electron density of a blob may be up to ten times greater than that of the background [16]. The size of a blob can reach tens of kilometers. Blobs can bend the HF waves from the great-circle bearing by a considerable amount. To illustrate this, a blob having a density increase of  $2 \times 10^5 \text{ cm}^{-3}$  in a horizontal range of 300 m, could refract a 10 MHz wave by  $40^\circ$  in bearing at each side of the path ( $80^\circ$  total) [16]. This represents an increase of 30% in path length with respect to the great-circle path; and, for a 2000 Km path, it means a multipath spread of 2.0 ms.

Scatter observations [16] indicate that the blobs are usually extended in the East-West direction rather than the North-South one. In other words, blobs occasionally show variations in latitudinal cross section as a function of longitude.

Instabilities occur at the steep density gradients (walls) at the trailing edges of the blob and can scatter the HF waves. These are the small scale irregularities with subkilometer sizes.

#### d. Sporadic-E Effects

Sporadic-E ( $E_s$ ) ionization refers to transient areas of abnormally intense electron density. These areas are horizontally extended and located in the E region.  $E_s$  ionization occurs primarily during the winter-night period. It is very important, because it frequently supports high-latitude HF propagation in the 20 MHz region. The auroral  $E_s$  is a significant HF propagation mode for paths up to 2300 Km [19].

#### e. Electron Density Troughs

It is known [20] that the inner magnetosphere co-rotates with the earth, whereas the outer magnetosphere follows circulation patterns determined by the solar wind. The difference in the circulation patterns between the inner and outer magnetosphere results in the formation of a trough [20]. That is, the ionosphere tends to be depleted between the mid-latitude and high-latitude regions to form a "belt" of low electron density.

Troughs occur in every season but are a night-time phenomenon at geomagnetic latitudes between  $60^\circ$  and  $65^\circ$ .

## APPENDIX B ANTENNA RADIATION PATTERNS FOR PROPHET

AD>777

ANTENNA LABEL = 777 SLOPING VEE, ANGLE 90 DEG  
 TRANSMIT CAPABILITY = Y POLARIZATION = V BEAMWIDTH = 30.0  
 AZIMUTH PATTERN IS UNI-DIRECTIONAL

90 deg:	-11	-9	-8	-9	-11	-13	-21	-14	-13	-10	-6	-10	-9	-9	-26	-18	-16	-7	-7	-18	-3
70 deg:	-8	-6	-7	-7	-6	-10	-21	-25	-15	-8	-4	-6	-8	-6	-8	-17	-15	-14	-10	-7	-4
50 deg:	-8	-3	-3	-4	-4	-4	-4	-6	-12	-14	-9	-8	-6	-3	-1	-1	-3	-7	-10	-1	-1
40 deg:	-8	-3	-1	-1	-2	-3	-3	-2	-3	-5	-9	-12	-8	-6	-5	-4	-1	1	1	-11	1
20 deg:	-13	-7	-3	-2	0	0	0	1	1	1	3	3	3	3	1	-1	-2	-4	-5	-10	-1
6 deg:	-22	-16	-13	-10	-8	-7	-7	-6	-6	-5	-4	-3	-2	-1	-1	0	0	0	0	3	3
GW:	-38	-32	-28	-26	-24	-23	-22	-21	-21	-20	-19	-18	-17	-16	-15	-15	-15	-15	-15	-11	-10
Freq:	2	4	6	8	10	12	14	16	18	20	30										

AD>778

ANTENNA LABEL = 778 WHIP ANTENNA, TRANSMITTER  
 TRANSMIT CAPABILITY = Y POLARIZATION = V BEAMWIDTH = 360.0  
 AZIMUTH PATTERN IS OMNI-DIRECTIONAL

90 deg:	-40	-40	-40	-40	-40	-40	-40	-40	-40	-40	-40	-40	-40	-40	-40	-40	-40	-40	-40	-40	-40
70 deg:	-40	-38	-34	-31	-27	-24	-22	-20	-17	-17	-18	-20	-21	-20	-20	-19	-18	-17	-16	-25	-16
50 deg:	-40	-33	-29	-25	-21	-18	-15	-12	-10	-8	-10	-11	-13	-14	-15	-14	-13	-12	-10	-11	-16
40 deg:	-40	-31	-27	-23	-19	-16	-13	-10	-7	-5	-6	-8	-9	-11	-12	-12	-13	-11	-9	-7	-21
20 deg:	-40	-31	-27	-23	-19	-15	-12	-8	-5	-3	-3	-4	-5	-6	-7	-7	-8	-7	-7	-5	-8
6 deg:	-40	-36	-32	-28	-24	-20	-17	-13	-10	-8	-8	-8	-9	-10	-10	-11	-11	-10	-10	-10	-9
GW:	-40	-40	-40	-40	-37	-34	-30	-27	-23	-21	-21	-21	-22	-23	-24	-24	-24	-24	-23	-23	-23
Freq:	2	4	6	8	10	12	14	16	18	20	30										

AD>779

ANTENNA LABEL = 779 BUTTERNUT (XMITTER)  
 TRANSMIT CAPABILITY = Y POLARIZATION = V BEAMWIDTH = 360.0  
 AZIMUTH PATTERN IS OMNI-DIRECTIONAL

90 deg:	-40	-40	-40	-40	-40	-40	-40	-40	-39	-39	-39	-39	-39	-40	-40	-40	-40	-40	-40	-35		
70 deg:	-27	-24	-21	-19	-18	-17	-16	-15	-14	-13	-12	-12	-13	-13	-13	-14	-14	-16	-18	-15	-9	
50 deg:	-21	-18	-16	-14	-12	-11	-10	-9	-8	-7	-6	-6	-6	-6	-6	-6	-6	-7	-8	-10	-6	
40 deg:	-20	-17	-14	-13	-11	-10	-9	-8	-7	-6	-5	-4	-4	-4	-4	-4	-4	-4	-4	-6	-5	
20 deg:	-19	-16	-14	-12	-10	-9	-8	-7	-6	-5	-4	-3	-3	-2	-2	-1	-1	-1	-1	0	0	
6 deg:	-22	-20	-17	-16	-15	-14	-13	-12	-11	-10	-8	-8	-8	-7	-7	-6	-6	-5	-5	-4	-3	
GW:	-33	-31	-30	-28	-27	-26	-25	-24	-24	-23	-21	-21	-21	-21	-20	-20	-19	-19	-19	-18	-17	-16
Freq:	2	4	6	8	10	12	14	16	18	20	30											

Figure 35. Radiation patterns, in terms of total gain (dB), of sloping-vee (code 777), whip (code 778) and "Butternut" (code 779) antennas utilized by Prophet.

# APPENDIX C NEC DATA SET FOR THE SLOPING-VEE ANTENNA

```
CE SLOPING VEE ANTENNA (ANGLE VEE 90 DEG.)
GW1,3,69.62,69.62,-1.,69.62,69.62,0.,.001,
GW2,3,69.62,69.62,0.,69.62,69.62,.6,.001,
GW3,41,69.62,69.62,.6,0.,0.,18.,.001,
GW4,41,0.,0.,18.,-69.62,69.62,.6,.001,
GW5,3,-69.62,69.62,.6,-69.62,69.62,0.,.001,
GW6,3,-69.62,69.62,0.,-69.62,69.62,-1.,.001
GE-1,
FR0,1,0,0,12.,1.,
GN2,0,0,0,30.,.01,
LD0,2,2,2,600.,0.,0.,
LD0,5,2,2,600.,0.,0.,
EX0,3,41,00,1.,0.,
EX0,4,1,00,1.,0.,
PL3,1,0,4
RP0,181,1,1001,-90.,90.,1.,0.,0.,
XQ0,
EN
```

Figure 36. NEC dataset for the simulation of sloping-vee antenna.

## LIST OF REFERENCES

1. D.B. Sailors, Operators Manual for the United States Coast Guard, Advanced PROPHET System, Naval Ocean Systems Center, San Diego 1987.
2. G.J. Burke, A.J. Pojio, Numerical Electromagnetics Code(NEC)-Method of Moments, Lawrence Livermore Laboratory, January 1981.
3. M. Tsolekas, "A Comparison of High-latitude Ionospheric Propagation Predictions from IONCAP-PC 2.5 With Measured Data," Master's thesis, Naval Postgraduate School, Monterey, California, 1990.
4. Ionospheric Physics Group, "Noncentric: Automatic Signal Recognition," Leicester University U.K., 4 December 1989.
5. A.A. Tomko, "Statistical Analysis of the Prediction Accuracy of HF Propagation Models," presented at the National Radio Science Meeting, Boulder, Colorado, January 1989.
6. Helen E. Hoffey, "Geomagnetic and Solar Data," Journal of Geophysical Research, Vol. 93, No A12, p. 14732, December 1988.
7. Helen E. Hoffey, "Geomagnetic and Solar Data," Journal of Geophysical Research, Vol. 94, No A1, p. 511, January 1989.
8. Helen E. Hoffey, "Geomagnetic and Solar Data," Journal of Geophysical Research, Vol. 94, No A6, p. 7020, June 1989.
9. Helen E. Hoffey, "Geomagnetic and Solar Data," Journal of Geophysical Research, Vol. 94, No A7, p. 9161, July 1989.
10. John Griffiths, Radio Wave Propagation and Antennas, Prentice-Hall International (UK) Ltd., 1987.
11. Nicholas M. Maslin, HF Communications: A Systems Approach, Plenum Press, New York, 1987.
12. Gerhard Braun, Planning and Engineering of Shortwave Links, Siemens, Berlin, 1986.

13. Kenneth Davies, Ionospheric Radio Propagation, National Bureau of Standards, 1965.
14. A.J. Foppiano and P.A. Bradley, "Prediction of Auroral Absorption of High-frequency Waves at Oblique Incidence," Telecommunication Journal, Vol. 50, pp. 547-560, 1983.
15. J.K. Hargreaves, M.T. Feeney, H. Ranta, A. Ranta, "On the Prediction of Auroral Radio Absorption on the Equatorial Side of the Absorption Zone," Journal of Atmospheric and Terrestrial Physics, Vol. 49, No. 3, pp. 259-272, 1987.
16. Radio Propagation Laboratory, Ottawa, Canada, "HF Communications and Remote Sensing in the High-latitude Region," by John S. Belrose, March 1987.
17. J.K. Hargreaves, "Auroral Absorption of HF Radio Waves in the Ionosphere: A review of Results from the First Decade of Riometry," Proceedings of the IEEE, Vol. 57, No. 8, pp. 1348-1373, August 1969.
18. D.K. Bailey, "Polar-cap Absorption," Planet. Space Sci., Vol. 12, pp. 495-541, 1964.
19. R.D. Hunsucker and H.F. Bates, "Survey of Polar and Auroral Region Effects on HF Propagation," Radio Science, Vol. 4, No. 4, pp. 347-365, April 1969.
20. Department of Environmental Science, University of Lancaster U.K., "The High-latitude Ionosphere: Dynamical Aspects and Models," by J.K. Hargreaves, 1987.

# INITIAL DISTRIBUTION LIST

	No Copies
1. Defense Technical Information Center Cameron Station Alexandria, VA 22304-6145	2
2. Library, Code 52 Naval Postgraduate School Monterey, CA 93943	2
3. Chairman, Code EC Department of Electrical and Computer Engineering Naval Postgraduate School Monterey, CA 93943	1
4. Professor W. R. Adler, Code EC/Ab Department of Electrical and Computer Engineering Naval Postgraduate School Monterey, CA 93943	5
5. Professor S. Jauregui, Code EC/Ja Department of Electrical and Computer Engineering Naval Postgraduate School Monterey, CA 93943	1
6. Professor W. R. Vincent, Code EC/Ja Department of Electrical and Computer Engineering Naval Postgraduate School Monterey, CA 93943	1
7. Dr. Joe Allen NOOA/WDC-A Boulder, CO 80303	1
8. Mr. Peter Bradley Rutherford Appleton Lab Chilton, Didcot, Oxon U.K., OX11 0QW	1
9. Wayne Bratt Naval Ocean Systems Center Code 772 San Diego, CA 92152-5000	1

10. Professor James K. Breakall 1  
Pennsylvania State University  
318 EE EAST/COMM & SPACE SCI LAB  
University Park, PA 16802
11. Jurgen Buchau 1  
GL/AFSC-LIS  
Hanscom AFB, MA 01731
12. Rex Buddenberg 1  
Commandant US Coast Guard (G-TES)  
Washington, DC 20593
13. Lt. Steve Carder 1  
Naval Security Group Command, Code GX  
3801 Nebraska Ave. NW  
Washington, DC 20393-5220
14. Dr. T. Dambolt 1  
Forschungs Inst. Der BDP  
Postfach 500  
Darmstadt, West Germany D-6100
15. Dr. A. J. Ferraro 1  
Pennsylvania State University  
Ionosphere Research Lab  
University Park, PA 16802
16. Dr. Raymond A. Greenwald 1  
John Hopkins University, Appl. Phys. Lab  
John Hopkins Rd,  
Laurel, MD 20723-6099
17. George Hagn 1  
SRI International  
1611 N. Kent str.  
Arlington, VA 22209
18. Dr. John K. Hargreaves 1  
University of Lancaster, E.S. Dept.  
Bailrigg, Lancaster U.K., LA2 8LL
19. William Hickey 1  
Ball Aerospace Corp.  
Box 1062 (TT4)  
Boulder, CO 80306
20. Dr. Robert Hunsucker 1  
R P Consultants  
1618 Scenic Loop  
Fairbanks, AK 99709



21. Dr. Tudor B. Jones 1  
University of Leicester, Dept. of Physics  
Leicester U.K., LEI 7RH
22. Mrs. Joanne Joselyn 1  
Hiraiso Solar-Terrestrial Res. Center  
3601 Isozoki  
Nakaminato, Ibaraki, Japan 311-2
23. Dave Lambert 1  
Naval Ocean Systems Center  
Code 772  
San Diego, CA 92152-5000
24. George Lane 1  
Voice of America/ESAP  
WJ Cohen Bldg Room 4230  
Washington, DC 20547
25. Dr. E. Kriezis 1  
Aristotle University of Thessaloniki  
Dept. of EE/FAC of Tech  
Thessaloniki 54006, Greece
26. Adolf K. Paul 1  
Naval Ocean Systems Center  
Code 544  
San Diego, CA 92152-5000
27. Dr. C. Naldoupis 1  
University of Crete, Physics Dept.  
Iraklion Crete, Greece
28. Jane Perry 1  
1921 Hopefield Rd  
Silver Spring, MD 20904
29. Dr. Art Richmond 1  
NCAR/WDC-A  
Box 3000  
Boulder, CO 80307
30. Robert Riegel 1  
SR 177B  
Ridge, MD 20680
31. Daniel P. Roesler 1  
Rockwell Int. CDC/MS 137-138  
1731 Southview Dr NW  
Cedar Rabbits, IA 52405

32. R. B. Rose 1  
Naval Ocean Systems Center, Code 542  
San Diego, CA 92152-5000
33. David B. Sailors 1  
Naval Ocean Systems Center, Code 542  
271 Catalina Blvd  
San Diego, CA 92152-5000
34. Dr. R. W. Schunk 1  
Utah State University, Ctr for Atmospheric  
Space Sciences/UMC 4405  
Logan, UT 84322-4405
35. Dennis Sheppard 1  
Naval Security Group Command/Code GX  
3801 Nebraska Ave NW  
Washington, DC 20393-5220
36. William Sherill 1  
S W Res Inst  
Op Drawer 28510  
San Antonio, TX 78284
37. Georgellen Smith 1  
SRI International  
333 Ravenswood Ave  
Menlo Park, CA 94025
38. Dr. H. Soicher 1  
US Army Comm-Elec Command  
AMSEL-RD-C3-TR-4  
FT Monmouth, NJ 07703-5202
39. Frank G. Steward 1  
US Department of Commerce  
NTIA/ITS.S3, 325 Broadway  
Boulder, CO 80303
40. Lloyd Teeters 1  
ITS  
325 Broadway  
Boulder, CO 80303
41. Dr. Al Tomko 1  
The Johns Hopkins University, APL/MS-13N574  
Johns Hopkins Rd  
Laurel, MD 20723

- |   |   |
|---|---|
| 42. Captain Vlahakis<br>Hellenic AF Research Tech Ctr KETA<br>PO Terpsitheas, Glyfada 16501<br>Athens, Greece | 1 |
| 43. LCDR Carl Wales<br>Naval Ocean Systems Center<br>Arctic Submarine Lab<br>San Diego, CA 92152              | 1 |
| 44. Empassy of Greece<br>Naval Attache<br>2228 Massachusetts Ave, NW<br>Washington, DC 20008                  | 2 |
| 45. Lt. George Giakoumakis<br>Tavronitis, Hania<br>Crete, Greece  | 1 |
| 46. Lt. Stefanos Gikas<br>72 Reppa str.<br>Papagos 15669<br>Athens, Greece                                    | 4 |